Chapter 2
Micromechanical Models for Auxetic Materials

Abstract This chapter provides a survey of micromechanical models that seek to predict and explain auxetic behavior, based on re-entrant microstructures, nodule-fibril microstructure, 3D tethered-nodule model, rotating squares, rectangles, triangles and tetrahedrals models, hard cyclic hexamers model, missing rib models, chiral and anti-chiral models, interlocking hexagon model, and the "egg rack" model. All the micromechanical models exhibit a common trait—auxeticity is highly dependent on the microstructural geometry. In some of the micromechanical geometries, comparisons between analytical results have been made with experimental or computational results.

Keywords Analytical models · Computational models · Effective elastic properties · Geometrical models · Micromechanics

2.1 Introduction

Figure 1.3.2 summarizes a few typical models which have been adopted to explain auxetic behavior. This chapter explores the micromechanics for some of these models in greater detail, with special emphasis on the adopted geometrical models and the analytical closed-form solutions.

2.2 Re-entrant Open-Cell Microstructure

Masters and Evans (1996) proposed an auxetic behavior based on the traditional 2D re-entrant structure shown in Fig. 2.2.1a, which is a hexagonal array of honeycomb structure (Gibson and Ashby 1988). With reference to Fig. 2.2.1b, the honeycomb is auxetic if θ is positive (unit cell possesses re-entrant shape) and conventional if θ

T.-C. Lim, *Auxetic Materials and Structures*, Engineering Materials,
DOI 10.1007/978-981-287-275-3_2

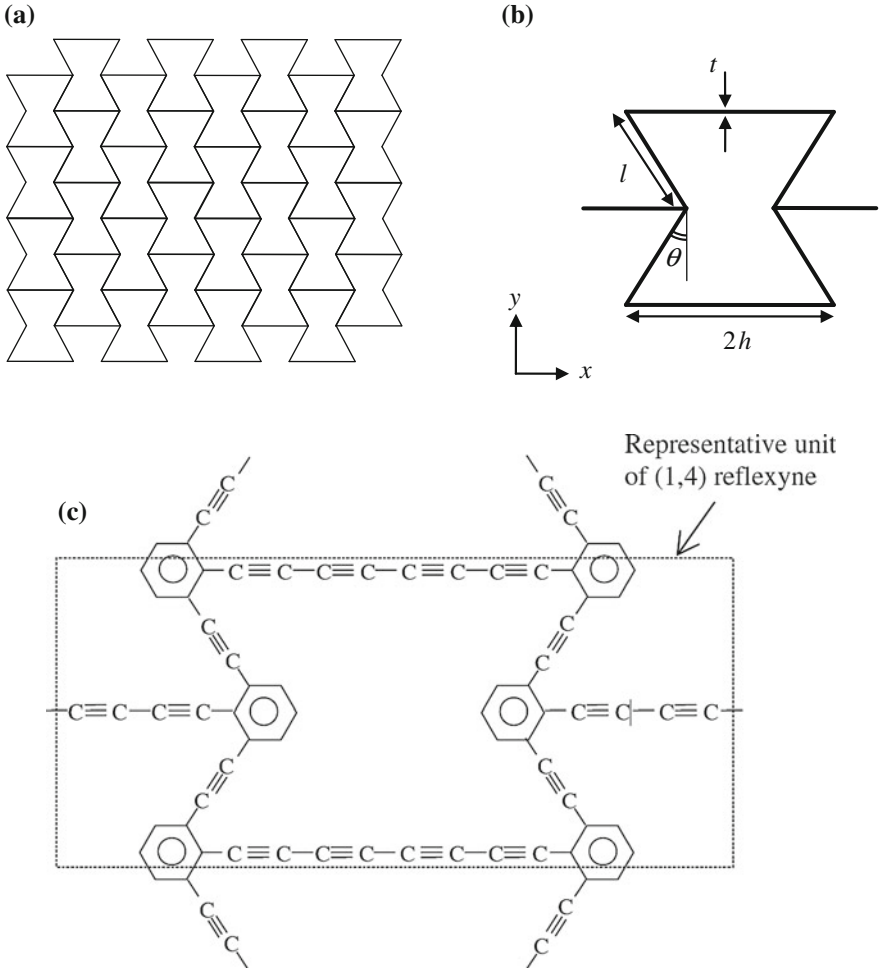

Fig. 2.2.1 **a** A 2D re-entrant structure, **b** geometry used by Smith et al. (2000), and a molecular re-entrant structure introduced by Evans et al. (1991)

is negative (unit cell possesses hexagonal shape), with the Poisson's ratio and Young's modulus in the direction of loading given by Smith et al. (2000)

$$v_{12} = \frac{\sin\theta(h/l + \sin\theta)}{\cos^2\theta} \tag{2.2.1}$$

and

$$E_1 = k\frac{(h/l) + \sin\theta}{b\cos^3\theta} \tag{2.2.2}$$

where the h is the half length of the horizontal rib, l is the length of the inclined rib, and t is the thickness of the rib, as shown in Fig. 2.2.1b, while b is the depth of the cell ribs not shown in Fig. 2.2.1b. The parameter k has been given as

$$k = E_s b \left(\frac{t}{l}\right)^3 \tag{2.2.3}$$

where E_s is the Young's modulus of the rib material. Results of this model are presented in Sect. 2.9 together with the missing rib model. It is also of interest to note that a similar structure has been introduced by Evans et al. (1991), as shown in Fig. 2.2.1c.

Based on the idealized re-entrant unit cell shown in Fig. 2.2.2a, Choi and Lakes (1995) proposed the corresponding geometry shown in Fig. 2.2.2b for analysis. The resultant Poisson's ratio at infinitesimal strain is

$$\nu_{elastic} = -\frac{\sin(\varphi - \pi/4)}{\cos(\varphi - \pi/4)} \tag{2.2.4}$$

where the angle φ is defined in Fig. 2.2.2b, while the Poisson's ratio at large strain after plastic hinge formation is given as

$$\nu_{plastic} = \frac{\cos(\varphi - \pi/4) - \cos(\varphi - \pi/4 - \theta)}{\sin(\varphi - \pi/4) - \sin(\varphi - \pi/4 - \theta)} \tag{2.2.5}$$

where θ refers to the clockwise angular rotation of cell rib BC.

The Poisson's ratio variation upon strain during elastic-plastic deformation was given by Choi and Lakes (1995) as

$$\nu_{elasto-plastic} = \nu_y - \varepsilon_{ex} \frac{1 - \cos\eta}{2\varepsilon_x} \tag{2.2.6}$$

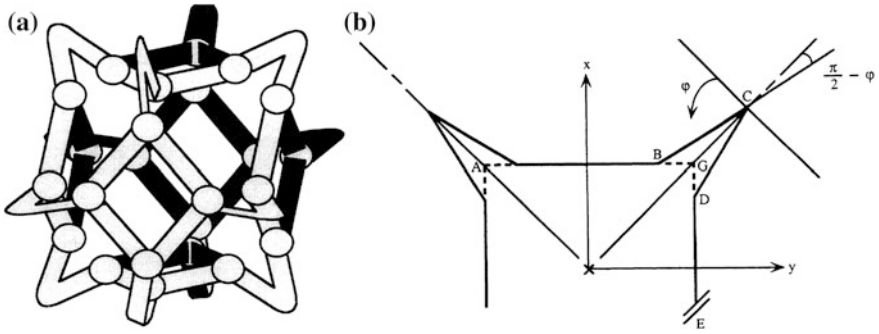

Fig. 2.2.2 **a** An idealized re-entrant unit cell, and **b** a zoomed-in view of the geometry adopted by Choi and Lakes (1995). Reprinted by permission of SAGE

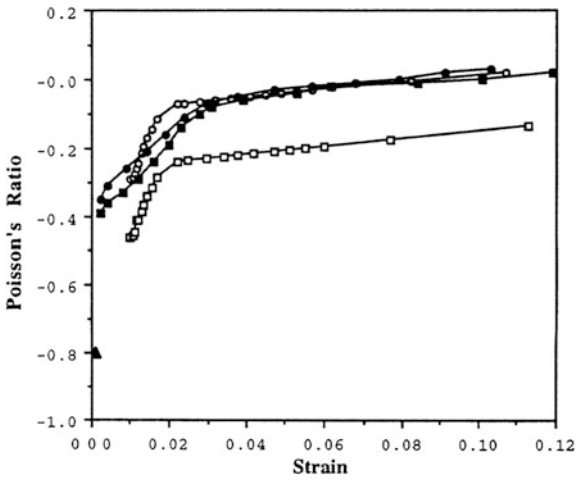

Fig. 2.2.3 Comparison of the modeling result by Choi and Lakes (1995) to the experimental data for copper foam: open symbols, modeling; solid symbols, experiments (Choi and Lakes 1992); circles, volumetric compression ratio 2.0; squares, volumetric compression ratio 2.5; triangle, optical test result, volumetric compression ratio 2.13. Reprinted by permission of SAGE

in which

$$\varepsilon_x = \frac{1}{\sqrt{2}} \frac{\sin(\varphi - \pi/4) - \sin(\varphi - \pi/4 - \theta)}{1 + \sin(\pi/2 - \varphi)} = \varepsilon_{ex} \frac{\delta}{\delta_e} \tag{2.2.7}$$

and

$$\eta = \frac{P_e}{P} \left(3 - \frac{P}{P_e} - 2\sqrt{3 - 2\frac{P}{P_e}} \right) \tag{2.2.8}$$

where v_y is the Poisson's ratio at initial yielding, ε_x is the strain in the x-direction, ε_{ex} is the x-component of strain at initial yielding, δ is the deflection, δ_e is the deflection at initial yielding, P is the load, and P_e is the load at initial yielding. A comparison between the predicted and measured Poisson's ratio versus strain for copper foam is shown in Fig. 2.2.3 based on the assumption of $\varepsilon_{ex} = 1\,\%$.

2.3 Nodule Fibril Microstructure—Hinging, Flexure and Stretching Modes of Fibrils

The nodule-fibril microstructural model proposed by Alderson and Evans (1995) considers deformation by fibril hinging mode, fibril flexure mode and fibril stretching mode separately. With reference to Fig. 2.3.1, the idealized nodule takes

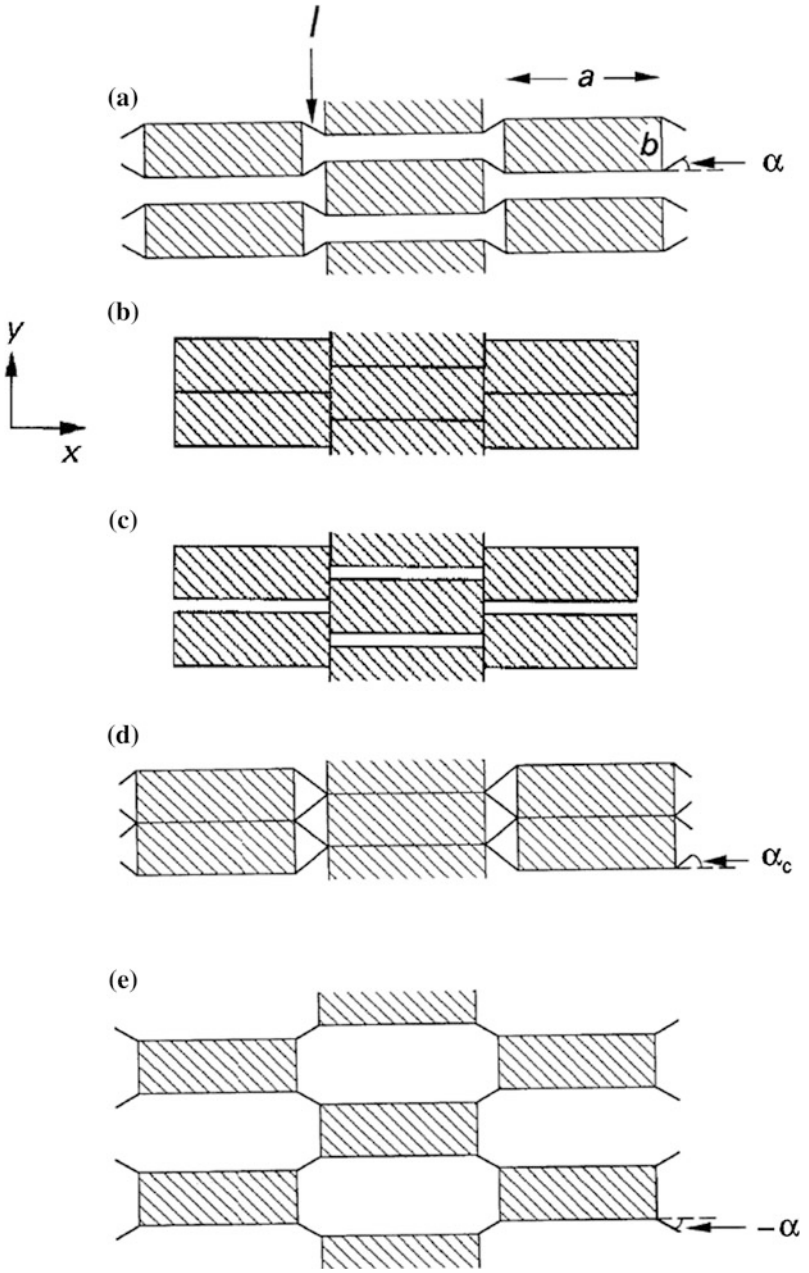

Fig. 2.3.1 Schematic diagram of the nodule-fibril (NF) model, showing **a** general parameters in a partially extended network, **b** fully densified network with $l = b/2$, $\alpha_0 = 90°$, and undeformed, partially open networks resulting from **c** $l < b/2$ with nodules in contact in x direction, **d** $l > b/2$ with nodules in contact in y direction, and **e** negative fibril angle (Alderson and Evans 1995, 1997). (With kind permission from Springer Science+Business Media)

a rectangular shape with major axis length a and minor axis length b, with the fibril geometry defined by its length l inclined at an angle α to the x-axis. Under tensile stress in the x-direction, the fibrils hinge, thereby reducing the angle of α until a minimum of $\alpha = 0°$.

Schematic diagrams for analyzing deformation by the fibril hinging mode under tension in the x direction and under compression in the y direction are shown in Fig. 2.3.2a, b respectively. Based on this analysis by Alderson and Evans (1995), the Poisson's ratio and Young's moduli due to fibril hinging were obtained as

$$v_{xy} = -\frac{\cos\alpha(a + l\cos\alpha)}{\sin\alpha(b - l\sin\alpha)} = \frac{1}{v_{yx}} \tag{2.3.1}$$

$$E_x = \frac{K_h}{l^2\sin^2\alpha}\left(\frac{a + l\cos\alpha}{b - l\sin\alpha}\right) \tag{2.3.2}$$

$$E_y = \frac{K_h}{l^2\cos^2\alpha}\left(\frac{b - l\sin\alpha}{a + l\cos\alpha}\right) \tag{2.3.3}$$

while the engineering Poisson's ratio and engineering Young's moduli were obtained as

$$v^e_{xy} = -\frac{\cos\alpha(a + l\cos\alpha_0)}{\sin\alpha(b - l\sin\alpha_0)} = \frac{1}{v^e_{yx}} \tag{2.3.4}$$

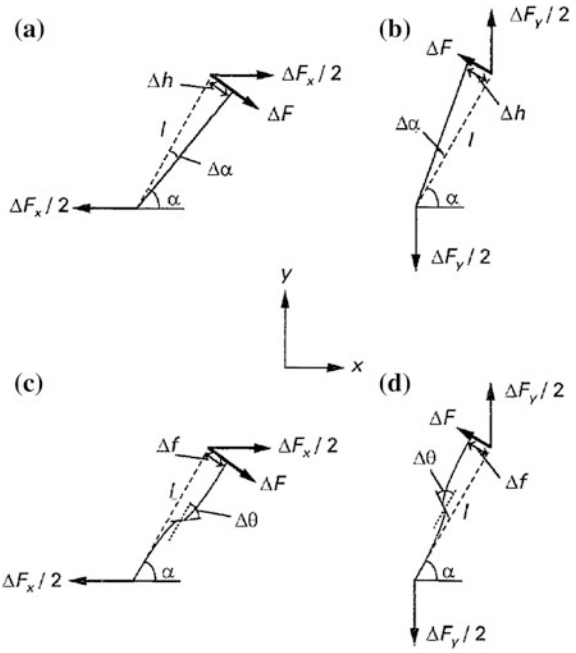

Fig. 2.3.2 **a** Fibril hinging under tension of the NF network in the x direction, **b** fibril hinging under compression of the NF network in the y direction, **c** fibril flexure under tension of the NF network in the x direction, and **d** fibril flexure under compression of the NF network in the y direction (Alderson and Evans 1995). With kind permission from Springer Science+Business Media

$$E_x^e = \frac{K_h}{l^2 \sin^2 \alpha}\left(\frac{a + l\cos\alpha_0}{b - l\sin\alpha_0}\right) \tag{2.3.5}$$

$$E_y^e = \frac{K_h}{l^2 \cos^2 \alpha}\left(\frac{b - l\sin\alpha_0}{a + l\cos\alpha_0}\right) \tag{2.3.6}$$

where the hinge force coefficient is defined from

$$l\Delta F = K_h \Delta\alpha \tag{2.3.7}$$

for an angular change $\Delta\alpha$ in response to a change in force ΔF while α_0 is the initial angle.

With reference to Fig. 2.3.2c, d, the analysis by Alderson and Evans (1995) based on fibril flexure gave the same expression of Poisson's ratio arising from fibril hinging as described in Eqs. (2.3.1) and (2.3.4). The Young's moduli due to fibril flexure were obtained as

$$E_x = \frac{3K_f}{l^2 \sin^2 \alpha}\left(\frac{a + l\cos\alpha}{b - l\sin\alpha}\right) \tag{2.3.8}$$

$$E_y = \frac{3K_f}{l^2 \cos^2 \alpha}\left(\frac{b - l\sin\alpha}{a + l\cos\alpha}\right) \tag{2.3.9}$$

while the engineering Young's moduli were obtained as

$$E_x^e = \frac{3K_f}{l^2 \sin^2 \alpha}\left(\frac{a + l\cos\alpha_0}{b - l\sin\alpha_0}\right) \tag{2.3.10}$$

$$E_y^e = \frac{3K_f}{l^2 \cos^2 \alpha}\left(\frac{b - l\sin\alpha_0}{a + l\cos\alpha_0}\right) \tag{2.3.11}$$

where the flexure force coefficient is defined from

$$K_f \Delta\theta = \Delta M = \frac{l\Delta F}{2} \tag{2.3.12}$$

and $\Delta\theta$ is the small change (i.e. $\Delta\theta = \tan\Delta\theta$) in the slope of the midpoint of the fibril with reference to the fibril orientation, as indicated in Fig. 2.3.2c, d.

Figure 2.3.3 illustrates the fibril stretching mode of deformation. Based on this nomenclature, Alderson and Evans (1995) derived the Poisson's ratio and Young's moduli as follows

$$\nu_{xy} = \frac{\sin\alpha(a + l\cos\alpha)}{\cos\alpha(b - l\sin\alpha)} = \frac{1}{\nu_{yx}} \tag{2.3.13}$$

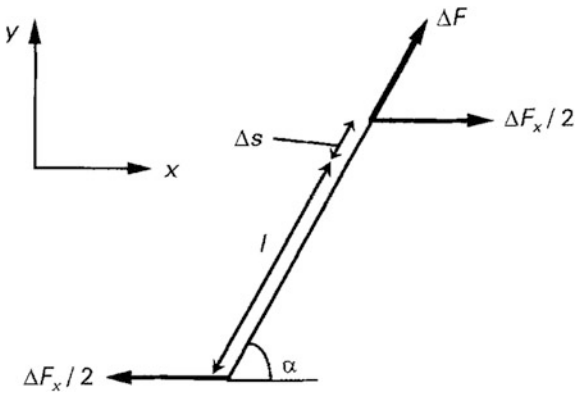

Fig. 2.3.3 Fibril extension under tension of the nodule-fibril network in the x direction (Alderson and Evans 1995). With kind permission from Springer Science+Business Media

$$E_x = \frac{K_s}{\cos^2 \alpha}\left(\frac{a + l\cos\alpha}{b - l\sin\alpha}\right) \tag{2.3.14}$$

$$E_y = \frac{K_s}{\sin^2 \alpha}\left(\frac{b - l\sin\alpha}{a + l\cos\alpha}\right) \tag{2.3.15}$$

while the corresponding engineering Poisson's ratio and Young's moduli were obtained as

$$v^e_{xy} = \frac{\sin\alpha(a + l\cos\alpha_0)}{\cos\alpha(b - l\sin\alpha_0)} = \frac{1}{v^e_{yx}} \tag{2.3.16}$$

$$E^e_x = \frac{K_s}{\cos^2 \alpha}\left(\frac{a + l\cos\alpha_0}{b - l\sin\alpha_0}\right) \tag{2.3.17}$$

$$E^e_y = \frac{K_s}{\sin^2 \alpha}\left(\frac{b - l\sin\alpha_0}{a + l\cos\alpha_0}\right) \tag{2.3.18}$$

where the stretching force coefficient is defined as

$$K_s = \frac{\Delta F}{\Delta s} \tag{2.3.19}$$

for an extension of Δs in response to ΔF.

Comparison between the analytical models and experimental results are shown in Figs. 2.3.4 and 2.3.5a, b for polytetrafluoroethylene (PTFE), and Fig. 2.3.5c for ultra-high molecular weight polyethylene (UHMWPE). Observation of Alderson and Evans (1995) noted that as α approaches 0° fibril stretching will become increasingly dominant, and this will have two effects: (a) the transition strain between the predominantly hinging and stretching modes will occur at a higher value of strain as a result of the increase in fibril length, and (b) the transition itself will become smeared over a range of strain.

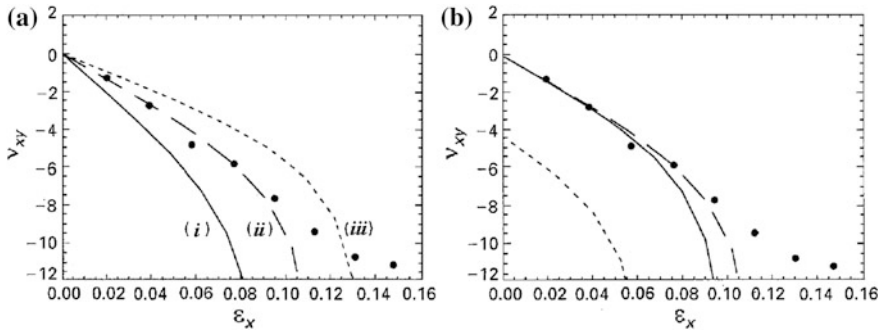

Fig. 2.3.4 **a** NF model ν_{xy} versus ε_x curves for the hinging mode of deformation in the NF model. Fits are for (*i*) $b/a = 0.2$, (*ii*) $b/a = 0.25$ and (*iii*) $b/a = 0.3$ with $l = b/2$ in all cases. Experimental data points (*filled circle*) for PTFE are also shown for comparison. **b** NF model ν_{xy} versus ε_x curves for the hinging mode of deformation in the NF model. Curves are for $b/a = 0.25$ with l = (*solid curve*) $0.11a$ ($<b/2$), l = (*dashed curve*) $0.125a$($=b/2$), and l = (*dotted curve*) $0.14a$($>b/2$). Experimental data points (*filled circle*) for PTFE are also shown for comparison (Alderson and Evans 1995). With kind permission from Springer Science+Business Media

The analysis by Alderson and Evans (1995) considers fibril hinging, flexure, and stretching separately, and found that fibril flexure and hinging result in exactly the same Poisson's ratio values and Young's modulus trends. Following up on this work, Alderson and Evans (1997) considered concurrenthinging and stretching deformation mechanisms to give the following properties based on loading in the *x*-direction

$$\nu_{xy} = \frac{[1 - l^2(K_s/K_h)]\sin\alpha\cos\alpha}{l^2(K_s/K_h)\sin^2\alpha + \cos^2\alpha}\left(\frac{a + l\cos\alpha}{b - l\sin\alpha}\right) \tag{2.3.20}$$

$$\nu^e_{xy} = \frac{[1 - l^2(K_s/K_h)]\sin\alpha\cos\alpha}{l^2(K_s/K_h)\sin^2\alpha + \cos^2\alpha}\left(\frac{a + l_0\cos\alpha_0}{b - l_0\sin\alpha_0}\right) \tag{2.3.21}$$

$$E_x = \left(\frac{l^2\sin^2\alpha}{K_h} + \frac{\cos^2\alpha}{K_s}\right)^{-1}\frac{a + l\cos\alpha}{b - l\sin\alpha} \tag{2.3.22}$$

$$E^e_x = \left(\frac{l^2\sin^2\alpha}{K_h} + \frac{\cos^2\alpha}{K_s}\right)^{-1}\frac{a + l_0\cos\alpha_0}{b - l_0\sin\alpha_0} \tag{2.3.23}$$

as well as in the *y*-direction

$$\nu_{yx} = \frac{[1 - l^2(K_s/K_h)]\sin\alpha\cos\alpha}{l^2(K_s/K_h)\cos^2\alpha + \sin^2\alpha}\left(\frac{b - l\sin\alpha}{a + l\cos\alpha}\right) \tag{2.3.24}$$

$$\nu^e_{yx} = \frac{[1 - l^2(K_s/K_h)]\sin\alpha\cos\alpha}{l^2(K_s/K_h)\cos^2\alpha + \sin^2\alpha}\left(\frac{b - l_0\sin\alpha_0}{a + l_0\cos\alpha_0}\right) \tag{2.3.25}$$

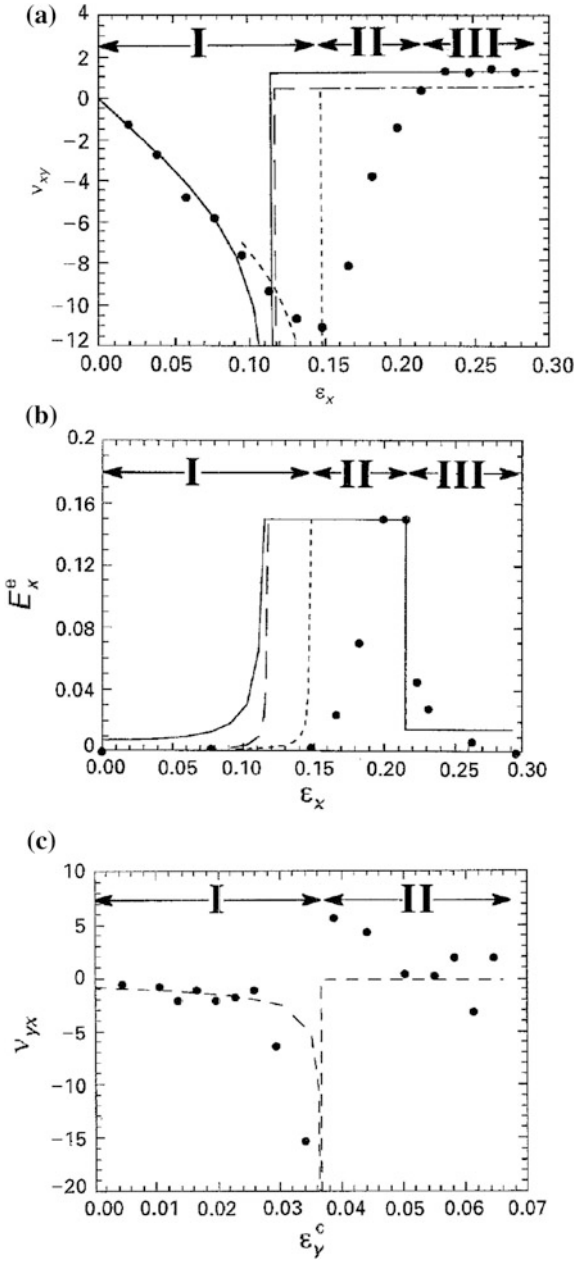

Fig. 2.3.5 **a** Experimental ν_{xy} versus ε_x data (*filled circle*) for PTFE. **b** Experimental E_x^e versus ε_x data (*filled circle*) for PTFE. Also shown are NF (hinging-plus-stretching) model calculations for $b/a = 0.25$, $l = b/2$ and $\alpha_0 = 90°$. Fit to the ν_{xy} data (*solid curve*), fit to the E_x^e data (*dashed curve*). NF model calculations for $b/a = 0.25$, $l = 0.16a$ and $\alpha_0 = 90°$ from fit to the E_x^e data (*dotted curve*). All NF model E_x^e predictions were normalized to the peak experimental E_x^e value of $E_x^e = 0.15$ GPa. **c** Experimental ν_{yx} versus ε_y^e data for UHMWPE by Alderson and Neale (1994) (*filled circle*). Also shown are NF (hinging-plus-stretching) model calculations for $a = b$ and $\alpha_0 = 40°$ for $l = 0.095b$ (*dashed curve*) (Alderson and Evans 1995). With kind permission from Springer Science+Business Media

$$E_y = \left(\frac{l^2\cos^2\alpha}{K_h} + \frac{\sin^2\alpha}{K_s}\right)^{-1} \frac{b - l\sin\alpha}{a + l\cos\alpha} \tag{2.3.26}$$

$$E_y^e = \left(\frac{l^2\cos^2\alpha}{K_h} + \frac{\sin^2\alpha}{K_s}\right)^{-1} \frac{b - l_0\sin\alpha_0}{a + l_0\cos\alpha_0} \tag{2.3.27}$$

For convenience Alderson and Evans (1997) defined an effective hinging force coefficient as

$$K_h^{eff} = \frac{K_h}{l^2}. \tag{2.3.28}$$

The elastic moduli were calculated for an arbitrary initial standard parameter set of $b/a = 1$, $l = 0.25a$, $K_s/K_h^{eff} = 10$, $\alpha = 45°$ and $\alpha_0 = 45°$. The effect of varying any one parameter on the behavior of the elastic moduli while keeping the others constant was examined. The effect of varying the force coefficients ratio, K_s/K_h^{eff}, is shown in Fig. 2.3.6 for the Poisson's ratio and Young's modulus due to loading in the x-direction. The Young's moduli data were normalized to the data calculated at $\alpha = 45°$, i.e.

$$E_x^* = \frac{E_x}{E_x(\alpha = 45°)} \tag{2.3.29}$$

because at $\alpha = 45°$ the Young's modulus due to hinging is equal to that due to stretching when $K_s = K_h^{eff}$.

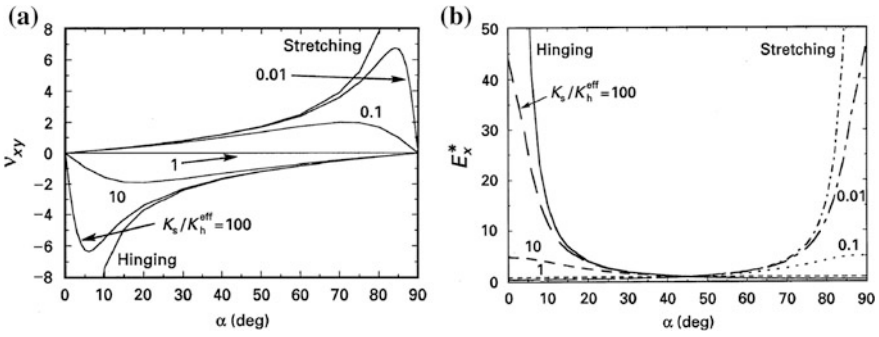

Fig. 2.3.6 **a** ν_{xy} versus α for the NF model employing concurrent fibril hinging and stretching mechanisms; **b** Normalized Young's modulus data E_x^* versus α for the NF model employing concurrent fibril hinging and stretching mechanisms; for each curve the data are normalized to the calculated value at $\alpha = 45°$, i.e. $E_x^* = E_x/E_x(\alpha = 45°)$. For (**a**) and (**b**), curves are for K_s/K_h^{eff} = 0.01, 0.1, 1, 10, 100 with stretching and hinging mechanisms acting independently, and calculations were performed with $b/a = 1$ and $l = 0.25a$ (Alderson and Evans 1997). With kind permission from Springer Science+Business Media

The effect of varying the geometrical parameters is illustrated in Fig. 2.3.7a. Figure 2.3.7b shows the variation of strain, in loading direction, with α, l_0/a and α_0, with a critical angle, α_c, as indicated in Fig. 2.3.1d, being defined as

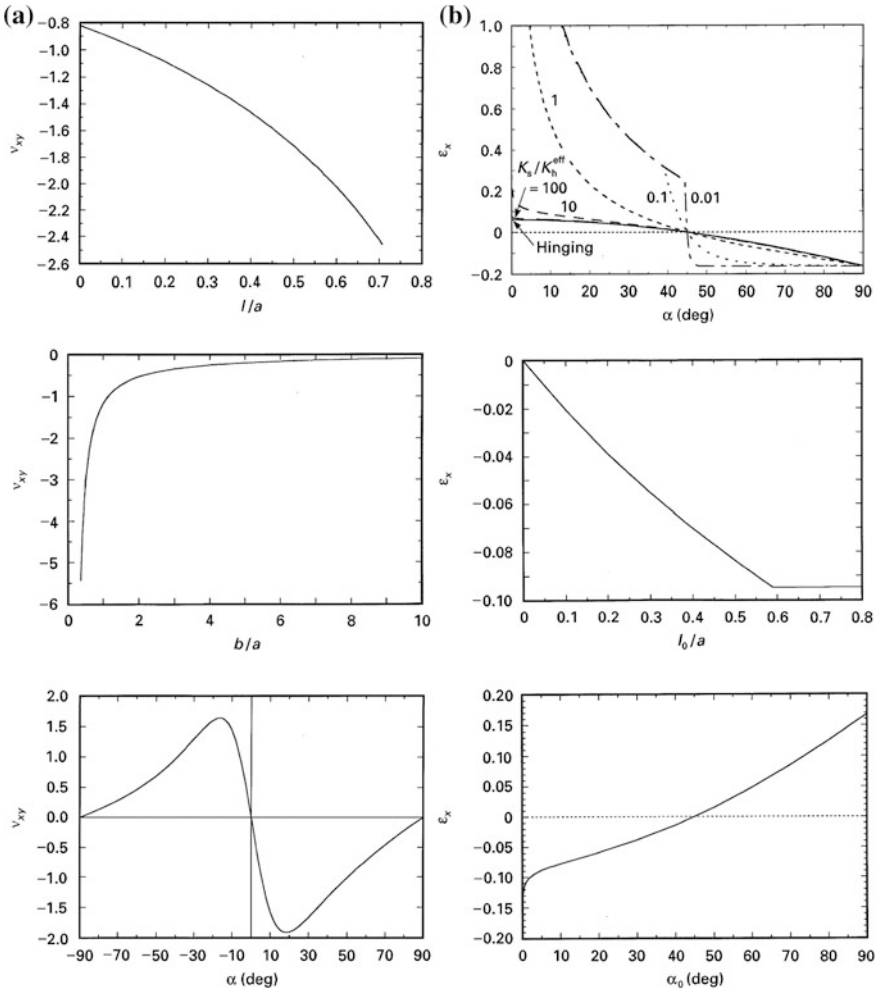

Fig. 2.3.7 **a** ν_{xy} trends for the NF model employing concurrent fibril hinging and stretching mechanisms calculated for a standard parameter set of b/a = 1, K_s/K_h^{eff} = 10, l = 0.25a and $\alpha = 45°$. ν_{xy} versus l/a (*top*), ν_{xy} versus b/a (*middle*), and ν_{xy} versus α (*bottom*). **b** ε_x trends under an x-directed load for the NF model employing concurrent fibril hinging and stretching mechanisms calculated for a standard parameter set of b/a = 1, l_0 = 0.25a, $\alpha_0 = 45°$, $\alpha = 45°$ and K_s/K_h^{eff} = 10. ε_x versus α with K_s/K_h^{eff} = 0.01, 0.1, 1, 10, 100 and ∞ (hinging) (*top*), ε_x versus l_0/a with $\alpha = 60°$ (*middle*), ε_x versus α_0 (*bottom*). Alderson and Evans (1997). With kind permission from Springer Science+Business Media

$$\sin \alpha_c = \frac{1}{2}\left(\frac{b}{l}\right). \tag{2.3.30}$$

From the plotted results, Alderson and Evans (1997) identified both the geometry and force coefficients involved in the deformation of the network microstructure as the determining factors of the elastic moduli.

Figure 2.3.8a shows that the elastic to plastic transition occurs when the fibril length has increased by 50 % of the initial value. The curves also show the same

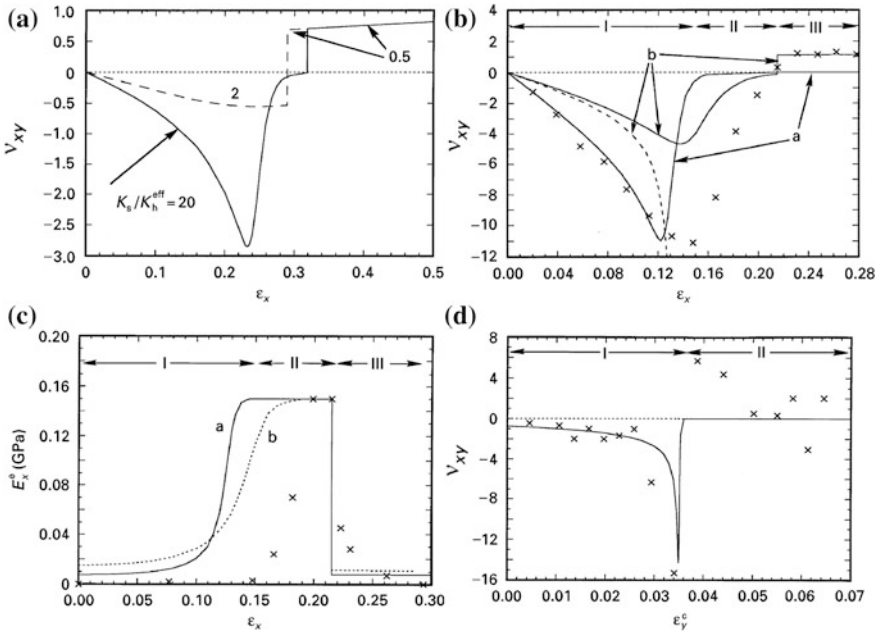

Fig. 2.3.8 **a** v_{xy} versus ε_x for the NF model employing concurrent fibril hinging and stretching mechanisms. b/a = 1, l_0 = 0.25a, $\alpha_0 = 90°$, and K_s/K_h^{eff} = 2 and 20 when $l \leq 1.5l_0$, and K_s/K_h^{eff} = 0.5 when $l \geq 1.5l_0$. **b** v_{xy} versus ε_x for the NF model employing fibril hinging (*dashed curve*) and concurrent fibril hinging and stretching (*solid curves*) mechanisms. Curves are for: "a" b = 0.25a, l = 0.125a, $K_s/K_h^{eff} = 20$ (elastic) and $K_s/K_h^{eff} = 1$ (plastic); "b" b = 0.40a, l = 0.14a, $K_s/K_h^{eff} = 10$ (elastic) and $K_s/K_h^{eff} = 0.65$ (plastic)). In all cases $\alpha_0 = 90°$ and K_s/K_h^{eff} is constant at the elastic or plastic value. Transition from elastic to plastic fibril extension was set to occur at l = 0.24a. Experimental v_{xy} data for PTFE by Caddock and Evans (1989) are also shown (*crosses*). **c** E_x^e versus ε_x for the NF model employing concurrent fibril hinging and stretching mechanisms. Model parameters as for (**b**). Experimental E_x^e data for PTFE are also shown (*crosses*). Model E_x^e data normalized to peak experimental value of E_x^e = 0.15 GPa. **d** v_{xy} versus compressive strain $\varepsilon_y^C (= -\varepsilon_y)$ for the NF model employing concurrent fibril hinging and stretching mechanisms (*solid curve*). Calculations are for $b = a$, l_0 = 0.09a, and $\alpha_0 = 40°$. K_s/K_h^{eff} = 1,000 throughout. Experimental v_{xy} data for UHMWPE are also shown (*crosses*). Alderson and Evans (1997). With kind permission from Springer Science+Business Media

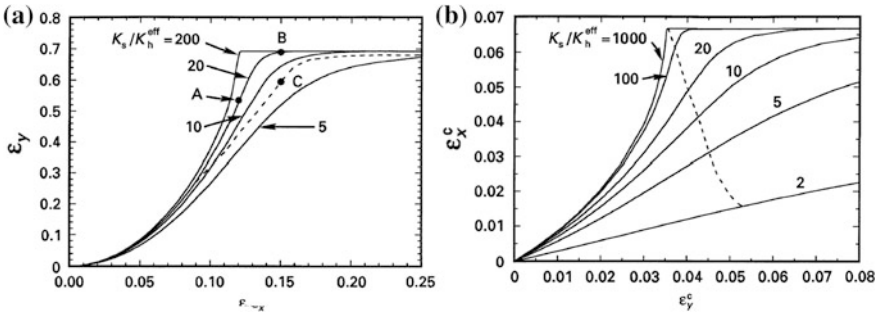

Fig. 2.3.9 **a** ε_y versus ε_x for the NF model employing concurrent fibril hinging and stretching mechanisms under an x-directed load. Calculations are for $b = 0.25a$, $l_0 = 0.125a$, $\alpha_0 = 90^\circ$ and K_s/K_h^{eff} = 200, 20, 10 and 5. *Dashed curve* corresponds to K_s/K_h^{eff} arbitrarily decreasing from $K_s/K_h^{eff} = 20$ as ε_x increases from $\varepsilon_x \approx 0.10$. **b** ε_x^C versus ε_y^C for the NF model employing concurrent fibril hinging and stretching mechanisms under a y-directed load. Calculations are for $b = a$, $l_0 = 0.09a$, $\alpha_0 = 40^\circ$ and K_s/K_h^{eff} = 1,000, 100, 20, 10, 5 and 2. The *dashed curve* illustrates the effect of decreasing K_s/K_h^{eff} from 1,000 to 2 in the strain range $0.036 < \varepsilon_y^C < 0.05$ (Alderson and Evans 1997). With kind permission from Springer Science+Business Media

general trends, v_{xy} becoming increasingly negative (from an initial value of zero at zero strain) as the strain increases, peaking at a strain of $\varepsilon_x \approx l/a$ before decreasing towards $v_{xy} \approx 0$ as ε_x increases further. Comparison with experimental results of PTFE by Caddock and Evans (1989) are shown in Fig. 2.3.8b, c for v_{xy} and E_x^e, respectively, while a comparison with experimental results of UHMWPE by Neale et al. (1993) and Alderson et al. (1997) is given in Fig. 2.3.8d (Alderson and Evans 1997). The characteristics of strain-dependent Poisson's ratio behavior for various K_s/K_h^{eff} are shown in Fig. 2.3.9 for tensile and compressive loadings, respectively.

2.4 Generalized 3D Tethered-Nodule Model

Based on the 3D tethered nodule, Gaspar et al. (2011) set up the following elastic property equations on the basis of idealized stretching model, the idealized ϕ hinging model, and the idealized θ hinging model. With reference to Fig. 2.4.1a, b, the projections along the x_i directions (for $i = 1, 2, 3$) are X_1, X_2 and X_3 respectively, with the connecting rods possessing equal length l while ϕ is the angle between the rods and the x_3 direction and θ is the angle that the projection of the rod in the $x_1 - x_2$ plane makes with the x_1 direction.

For an incremental force of dF_l, dF_θ and dF_ϕ that causes an incremental change of dl, $d\theta$ and $d\phi$ respectively, the stiffness k_l, k_θ and k_ϕ are defined as

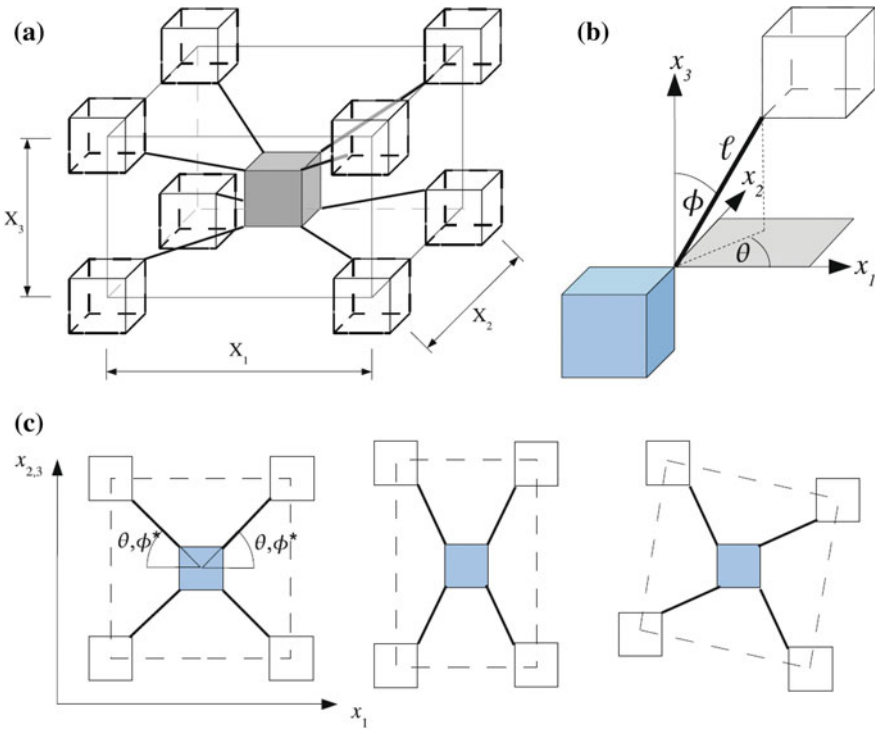

Fig. 2.4.1 Schematics for a generalized 3D tethered nodule, showing: **a** a central nodule connected to eight others via corner fibril, **b** geometrical description, and **c** a projection in the $x_1 - x_2$ axis or $x_1 - x_3$ axis with angle θ or projected angle ϕ^* marked on the left and on the right. Reference cell (*left*) and two different symmetry cases (*middle and right*) for deformation of the marked angle. In the first case (*middle*), the left and right angles change together. In the second case (*right*), the change of left and right angles have opposite signs (Gaspar et al. 2011). With kind permission from Springer Science+Business Media

$$k_l = \frac{dF_l}{dl} \tag{2.4.1}$$

$$k_\theta = \frac{dM_\theta}{d\theta} = \frac{ldF_\theta}{d\theta} \tag{2.4.2}$$

$$k_\phi = \frac{dM_\phi}{d\phi} = \frac{ldF_\phi}{d\phi} \tag{2.4.3}$$

respectively. Gaspar et al. (2011) obtained the following elastic moduli

$$E_1^l = \frac{2k_l}{\cos^2\theta\ \sin^2\phi}\left(\frac{X_1}{X_2X_3}\right) \tag{2.4.4}$$

$$E_2^l = \frac{2k_l}{\sin^2\theta\ \sin^2\phi}\left(\frac{X_2}{X_1X_3}\right) \tag{2.4.5}$$

$$E_3^l = \frac{2k_l}{\cos^2\phi}\left(\frac{X_3}{X_1X_2}\right) \tag{2.4.6}$$

$$v_{31}^l = \left(v_{13}^l\right)^{-1} = -\cos\theta\tan\phi\left(\frac{X_3}{X_1}\right) \tag{2.4.7}$$

$$v_{32}^l = \left(v_{23}^l\right)^{-1} = -\sin\theta\tan\phi\left(\frac{X_3}{X_2}\right) \tag{2.4.8}$$

$$v_{12}^l = \left(v_{21}^l\right)^{-1} = -\tan\theta\left(\frac{X_1}{X_2}\right) \tag{2.4.9}$$

based on idealized stretching model, the following elastic moduli

$$E_1^\phi = \frac{2k_\phi}{l^2\cos^2\theta\ \cos^2\phi}\left(\frac{X_1}{X_2X_3}\right) \tag{2.4.10}$$

$$E_2^\phi = \frac{2k_\phi}{l^2\sin^2\theta\ \cos^2\phi}\left(\frac{X_2}{X_1X_3}\right) \tag{2.4.11}$$

$$E_3^\phi = \frac{2k_\phi}{l^2\sin^2\phi}\left(\frac{X_3}{X_1X_2}\right) \tag{2.4.12}$$

$$v_{31}^\phi = \left(v_{13}^\phi\right)^{-1} = \cos\theta\ \cos\phi\left(\frac{X_3}{X_1}\right) \tag{2.4.13}$$

$$v_{32}^\phi = \left(v_{23}^\phi\right)^{-1} = \sin\theta\ \cos\phi\left(\frac{X_3}{X_2}\right) \tag{2.4.14}$$

$$v_{12}^\phi = \left(v_{21}^\phi\right)^{-1} = -\tan\theta\left(\frac{X_1}{X_2}\right) \tag{2.4.15}$$

based on idealized ϕ hinging model, and the following elastic moduli

$$E_1^\theta = \frac{2k_\theta}{l^2\sin^2\theta\ \sin\phi}\left(\frac{X_1}{X_2X_3}\right) \tag{2.4.16}$$

$$E_2^\theta = \frac{2k_\theta}{l^2\cos^2\theta\ \sin\phi}\left(\frac{X_2}{X_1X_3}\right) \tag{2.4.17}$$

$$v_{12}^\theta = \left(v_{21}^\theta\right)^{-1} = \cot\theta\left(\frac{X_1}{X_2}\right) \tag{2.4.18}$$

based on idealized θ hinging model (Fig. 2.4.2).

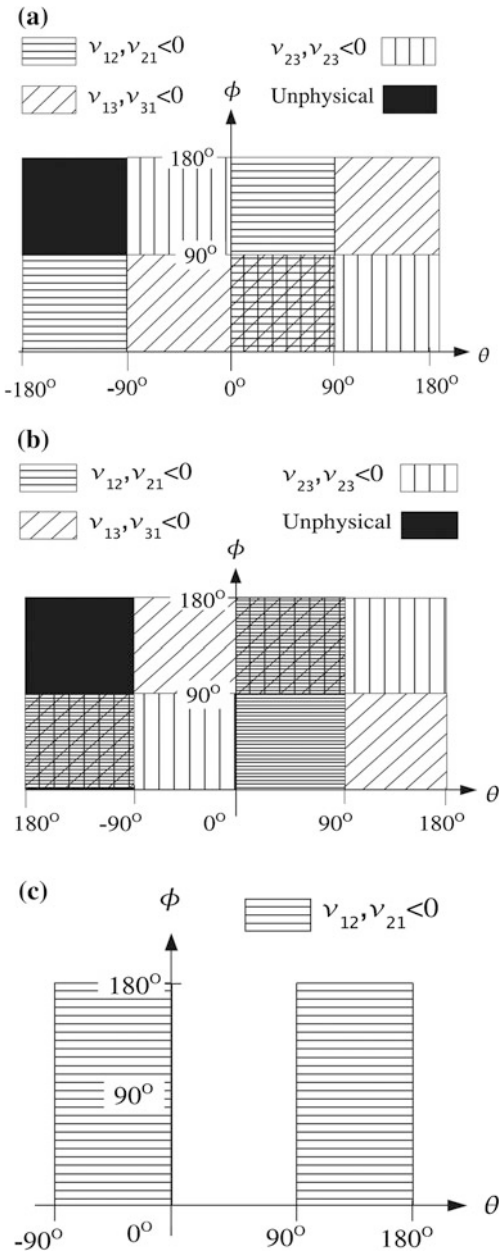

Fig. 2.4.2 Phase diagrams showing regions of negative Poisson's ratio: **a** for fibril stretching only, **b** for ϕ -deformation only, and **c** for θ-bending only by Gaspar et al. (2011). With kind permission from Springer Science+Business Media

The elastic moduli, taking into consideration all three modes of deformation are therefore given by Gaspar et al. (2011) as

$$\frac{1}{E_1} = \frac{X_2 X_3}{2X_1}\left(\frac{\cos^2\theta\ \sin^2\phi}{k_l} + \frac{l^2\cos^2\theta\ \cos^2\phi}{k_\phi} + \frac{l^2\sin^2\theta\ \sin\phi}{k_\theta}\right) \tag{2.4.19}$$

$$\frac{1}{E_2} = \frac{X_1 X_3}{2X_2}\left(\frac{\sin^2\theta\ \sin^2\phi}{k_l} + \frac{l^2\sin^2\theta\ \cos^2\phi}{k_\phi} + \frac{l^2\cos^2\theta\ \sin\phi}{k_\theta}\right) \tag{2.4.20}$$

$$\frac{1}{E_3} = \frac{X_1 X_2}{2X_3}\left(\frac{\cos^2\phi}{k_l} + \frac{l^2\sin^2\phi}{k_\phi}\right) \tag{2.4.21}$$

$$\nu_{12} = -\frac{X_1}{X_2}\frac{\frac{\sin\theta\sin\phi}{k_l} + \frac{l^2\sin\theta\cos\phi\cot\phi}{k_\phi} - \frac{l^2\sin\theta}{k_\theta}}{\frac{\cos\theta\sin\phi}{k_l} + \frac{l^2\cos\theta\cos\phi\cot\phi}{k_\phi} + \frac{l^2\sin\theta\tan\theta}{k_\theta}} \tag{2.4.22}$$

$$\nu_{21} = -\frac{X_2}{X_1}\frac{\frac{\cos\theta\sin\phi}{k_l} + \frac{l^2\cos\theta\cot\phi\cos\phi}{k_\phi} - \frac{l^2\cos\theta}{k_\theta}}{\frac{\sin\theta\sin\phi}{k_l} + \frac{l^2\sin\theta\cos\phi\cot\phi}{k_\phi} + \frac{l^2\cos\theta\cot\theta}{k_\theta}} \tag{2.4.23}$$

$$\nu_{13} = -\frac{X_1}{X_3}\frac{\frac{\cos\phi}{k_l} - \frac{l^2\cos\phi}{k_\phi}}{\frac{\cos\theta\sin\phi}{k_l} + \frac{l^2\cos\theta\cos\phi\cot\phi}{k_\phi} + \frac{l^2\sin\theta\tan\theta}{k_\theta}} \tag{2.4.24}$$

$$\nu_{23} = -\frac{X_2}{X_3}\frac{\frac{\cos\phi}{k_l} - \frac{l^2\cos\phi}{k_\phi}}{\frac{\sin\theta\sin\phi}{k_l} + \frac{l^2\sin\theta\cos\phi\cot\phi}{k_\phi} + \frac{l^2\cos\theta\cot\theta}{k_\theta}} \tag{2.4.25}$$

$$\nu_{31} = -\frac{X_3}{X_1}\frac{\frac{\cos\theta\sin\phi}{k_l} - \frac{l^2\cos\theta\sin\phi}{k_\phi}}{\frac{\cos\phi}{k_l} + \frac{l^2\sin\phi\tan\phi}{k_\phi}} \tag{2.4.26}$$

$$\nu_{32} = -\frac{X_3}{X_2}\frac{\frac{\sin\theta\sin\phi}{k_l} - \frac{l^2\sin\theta\sin\phi}{k_\phi}}{\frac{\cos\phi}{k_l} + \frac{l^2\sin\phi\tan\phi}{k_\phi}}. \tag{2.4.27}$$

2.5 Rotating Squares and Rectangles Models

An early account on auxetic behavior arising from the rotation of connected squares was given by Grima and Evans (2000), which exhibits $\nu = -1$. Using the geometrical model displayed in Fig. 2.5.1a, they obtained a stress strain relationship in 2D

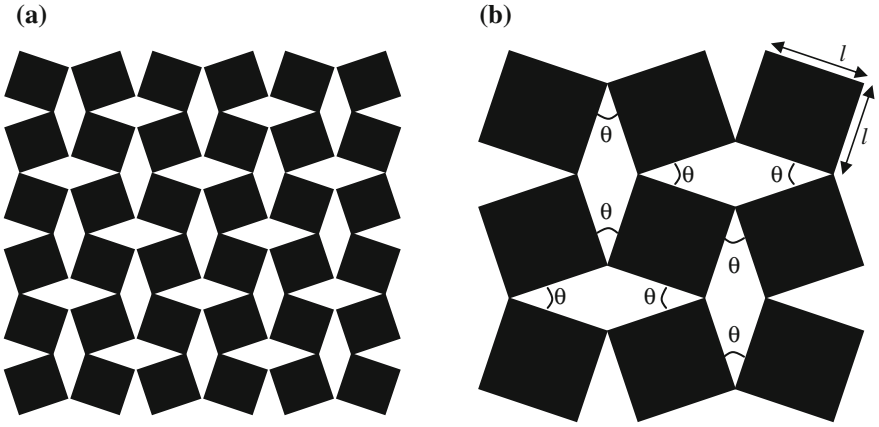

Fig. 2.5.1 Auxetic properties from connected rotating *squares*: **a** overview and **b** details

$$\begin{Bmatrix} \varepsilon_1 \\ \varepsilon_2 \\ \gamma_{12} \end{Bmatrix} = \begin{bmatrix} s_{11} & s_{12} & s_{13} \\ s_{21} & s_{22} & s_{23} \\ s_{31} & s_{32} & s_{33} \end{bmatrix} \begin{Bmatrix} \sigma_1 \\ \sigma_2 \\ \tau_{12} \end{Bmatrix}. \tag{2.5.1}$$

In general, the compliance matrix in Eq. (2.5.1) is expressed as

$$S = \begin{bmatrix} \frac{1}{E_1} & -\frac{\nu_{21}}{E_2} & \frac{\eta_{31}}{G_{12}} \\ -\frac{\nu_{12}}{E_1} & \frac{1}{E_2} & \frac{\eta_{32}}{G_{12}} \\ \frac{\eta_{13}}{E_1} & \frac{\eta_{23}}{E_2} & \frac{1}{G_{12}} \end{bmatrix} \tag{2.5.2a}$$

where η_{ij} are the shear coupling coefficients. For the particular case of rigid rotating squares of sides l and rotational stiffness constant of the hinge K_h, Grima and Evans (2000) gave the corresponding compliance matrix

$$S = \frac{1}{E} \begin{bmatrix} 1 & 1 & 0 \\ 1 & 1 & 0 \\ 0 & 0 & 0 \end{bmatrix} \tag{2.5.2b}$$

where the effective Young's modulus is

$$E = \frac{8K_h}{zl^2(1 - \sin\theta)} \tag{2.5.3}$$

in which θ is the angle defined in Fig. 2.5.1b and z is the thickness of the squares. Extending on this early work, Grima et al. (2007) investigated the auxetic behavior of semi-rigid rotating squares as shown in Fig. 2.5.2.

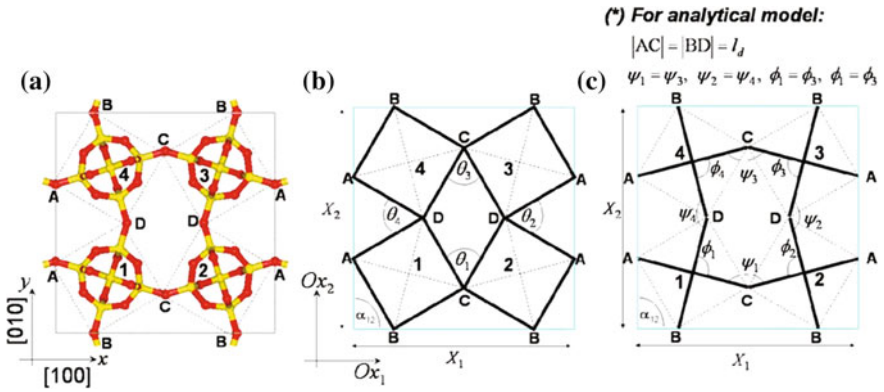

Fig. 2.5.2 Definition of the variables monitored defined relative to the zeolite THO (shown in (**a**)), with (**b**) the squares shown in *bold*, representing the original 'rotating squares' structure', and (**c**) the diagonals shown in *bold*, representing the new structure where the *squares* are replaced by their diagonals. Note that in the analytical model derived by Grima et al. (2007), $\psi_1 = \psi_3$, $\psi_2 = \psi_4$, $\phi_1 = \phi_3$ and $\phi_2 = \phi_4$. With kind permission from John Wiley & Sons

The analytical model for the on-axis elastic moduli were obtained by Grima et al. (2007) as

$$v_{12} = v_{21} = -\cot\left(\frac{\psi_1}{2}\right)\tan\left(\frac{\psi_2}{2}\right)\left[1 + 4\left(\frac{k_\psi}{k_\phi}\right)\right]^{-1} \tag{2.5.4}$$

$$E_1 = E_2 = \frac{8k_\psi(k_\phi + 2k_\psi)}{l_d^2 z(k_\phi + 4k_\psi)}\frac{\sin\left(\frac{\psi_2}{2}\right)}{\sin\left(\frac{\psi_1}{2}\right)\cos^2\left(\frac{\psi_2}{2}\right)} \tag{2.5.5}$$

$$G_{12} = \frac{\frac{k_\phi}{zl_d^2}}{\sin\left(\frac{\psi_1}{2}\right)\sin\left(\frac{\psi_2}{2}\right)\sin\phi_1} \tag{2.5.6}$$

where l_d is the diagonal length of the square (i.e. AC or BD in Fig. 2.5.2), while k_ψ and k_ϕ are the rotational stiffness constants that restrain changes to the angles ψ and ϕ, respectively, and z is the thickness of the squares. At zero strain (i.e. $\psi_1 = \psi_2 = \psi$) and initial angle of $\phi = \pi/2$, the elastic moduli expressions simplify to

$$v_{12} = v_{21} = -\left[1 + 4\left(\frac{k_\psi}{k_\phi}\right)\right]^{-1} \tag{2.5.7}$$

$$E_1 = E_2 = \frac{8k_\psi(k_\phi + 2k_\psi)}{l_d^2 z(k_\phi + 4k_\psi)}\sec^2\left(\frac{\psi}{2}\right) \tag{2.5.8}$$

$$G_{12} = \frac{k_\phi}{z l_d^2}\left[\sin^2\left(\frac{\psi}{2}\right)\right]^{-1}. \tag{2.5.9}$$

The off-axis elastic moduli at an angle ζ around the third direction are given by Grima et al. (2007) as

$$\frac{1}{E_1^\zeta} = \frac{m^4}{E_1} + \frac{n^4}{E_2} - m^2 n^2\left(2\frac{\nu_{12}}{E_1} - \frac{1}{G_{12}}\right) \tag{2.5.10}$$

$$\nu_{12}^\zeta = E_1^\zeta\left[(m^4 + n^4)\frac{\nu_{12}}{E_1} - m^2 n^2\left(\frac{1}{E_1} + \frac{1}{E_2} - \frac{1}{G_{12}}\right)\right] \tag{2.5.11}$$

$$\frac{1}{G_{12}^\zeta} = \frac{m^4 + n^4}{G_{12}} + 2m^2 n^2\left(\frac{2}{E_1} + \frac{2}{E_2} + \frac{4\nu_{12}}{E_1} + \frac{1}{G_{12}}\right) \tag{2.5.12}$$

where $m = \cos(\zeta)$ and $n = \sin(\zeta)$. Figure 2.5.3 shows the effect of k_ψ and k_ϕ in influencing the off-axis Poisson's ratio ν_{12}^ζ, while Fig. 2.5.4 compares the results of ν_{12}^ζ based on analytical model and molecular modeling results.

While the deformation by Grima et al. (2007) considers a change in the shape of the rotating squares, an alternate mode of deformation was later proposed by Grima et al. (2008) which deform solely through changes in length of the sides of the squares, i.e. the squares change their side lengths to become rectangles or squares of different sizes without changing the angles in the system. For this analysis, two possible orientations have been identified, as furnished in Fig. 2.5.5.

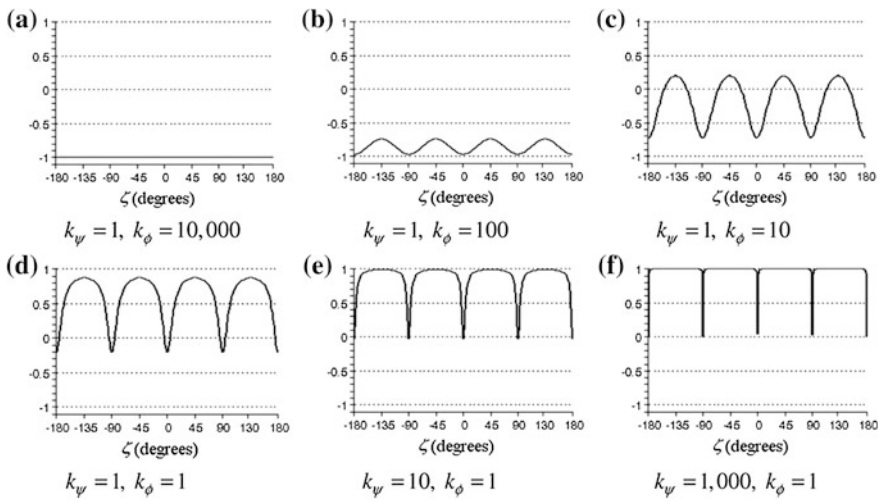

Fig. 2.5.3 Off-axis plots for various combinations of k_ψ and k_ϕ at $\psi = 145°$ (Grima et al. 2007). With kind permission from John Wiley & Sons

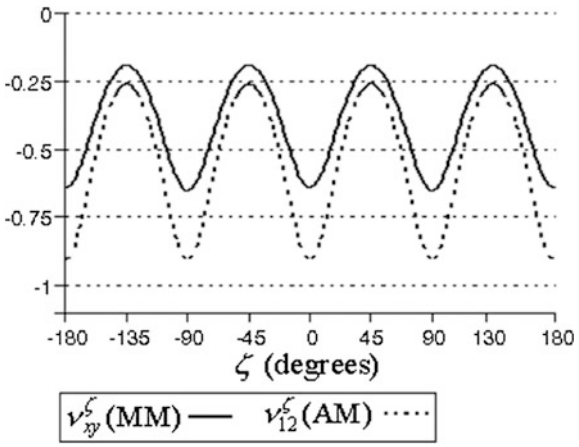

Fig. 2.5.4 A comparison of the off-axis Poisson's ratios ν_{12}^{ζ} for THO as predicted by molecular modeling (MM) using the Burchart force-field and the analytical model (AM) by Grima et al. (2007). With kind permission from John Wiley & Sons

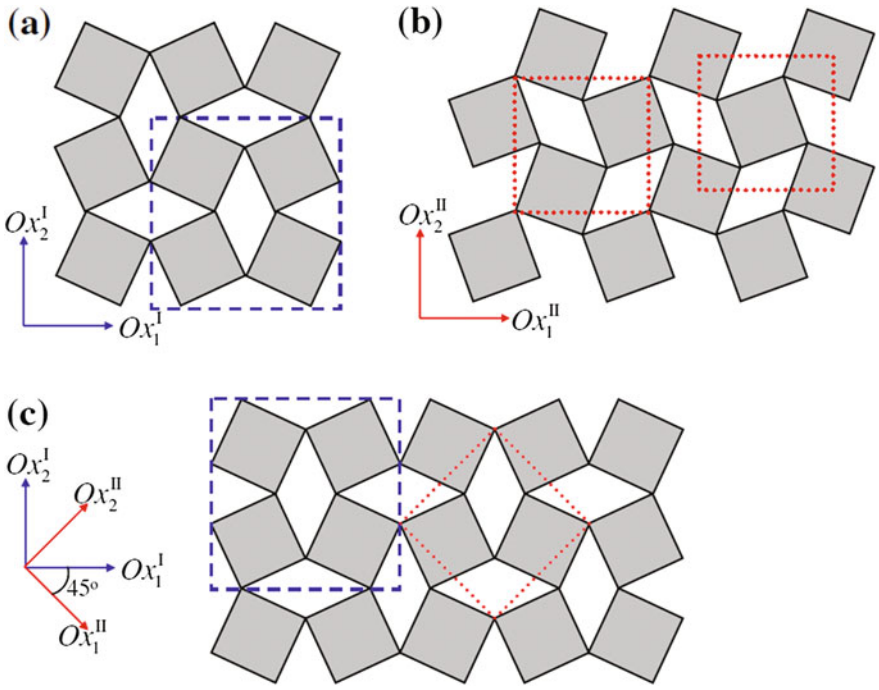

Fig. 2.5.5 The unit cells used to derive the mechanical properties of the 'stretching squares' model for **a** Orientation I and **b** Orientation II. **c** The geometric relation between the two orientations (Grima et al. 2008). With kind permission from Springer Science+Business Media

Suppose k_s is the stretching force constant per unit length of the "beam", which is a side of a square, and z is the thickness of the square, then with reference to Fig. 2.5.6, the elastic moduli have been given by Grima et al. (2008) as

$$\nu_{12}^{\mathrm{I}} = \nu_{21}^{\mathrm{I}} = -\sin\theta \tag{2.5.13}$$

$$E_1^{\mathrm{I}} = E_2^{\mathrm{I}} = \frac{2k_s}{z} \tag{2.5.14}$$

$$G_{12}^{\mathrm{I}} = \frac{k_s}{z(1+\sin\theta)} \tag{2.5.15}$$

for on-axis Orientation I, and

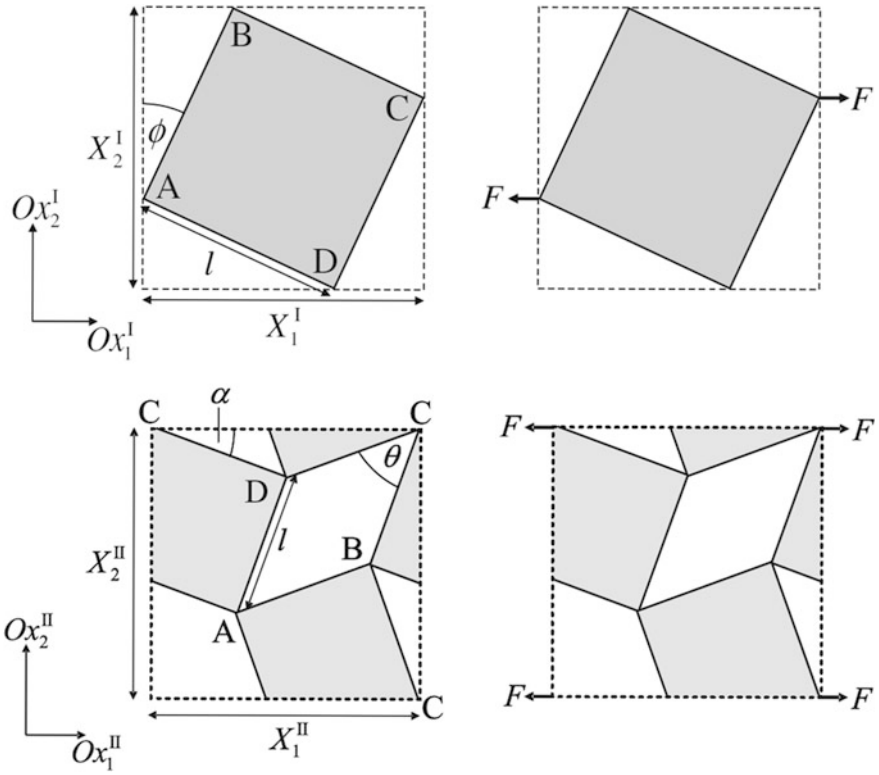

Fig. 2.5.6 One-fourth of an Orientation I unit cell showing dimensions (*top left*) and forces (*top right*), as well as an Orientation II unit cell showing dimensions (*bottom left*) and forces (*bottom right*) by Grima et al. (2008). With kind permission from Springer Science+Business Media

$$\nu_{12}^{\mathrm{II}} = \nu_{21}^{\mathrm{II}} = 0 \tag{2.5.16}$$

$$E_1^{\mathrm{II}} = E_2^{\mathrm{II}} = \frac{2k_s}{z(1+\sin\theta)} \tag{2.5.17}$$

$$G_{12}^{\mathrm{II}} = \frac{k_s}{z(1-\sin\theta)} \tag{2.5.18}$$

for on-axis Orientation 2.

Results for the elastic moduli on both orientations are shown in Fig. 2.5.7 at $k_s = 1$ and $z = 1$. From Eqs. (2.5.13) to (2.5.18), Grima et al. (2008) summarized the elastic properties in terms of compliance matrices as

$$S^{\mathrm{I}} = \frac{z}{2k_s}\begin{bmatrix} 1 & \sin\theta & 0 \\ \sin\theta & 1 & 0 \\ 0 & 0 & 2+2\sin\theta \end{bmatrix} \tag{2.5.19}$$

for Orientation I, and

$$S^{\mathrm{II}} = \frac{z}{2k_s}\begin{bmatrix} 1+\sin\theta & 0 & 0 \\ 0 & 1+\sin\theta & 0 \\ 0 & 0 & 2-2\sin\theta \end{bmatrix} \tag{2.5.20}$$

for Orientation II.

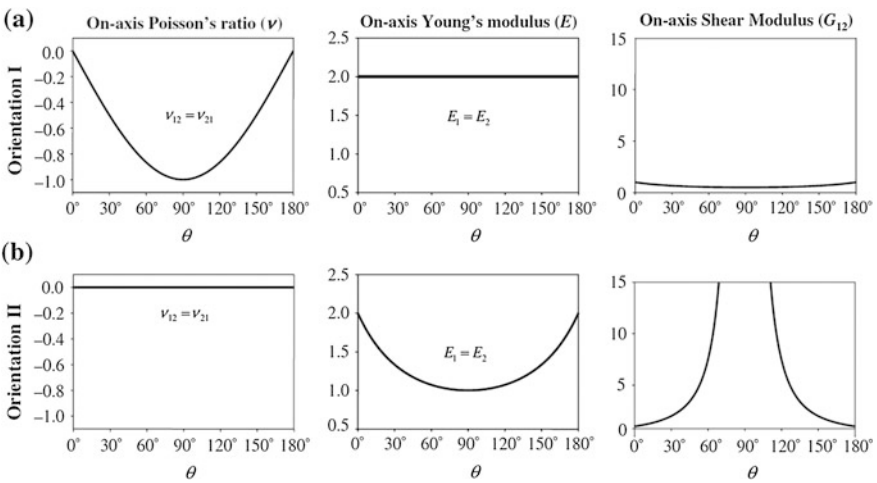

Fig. 2.5.7 The variation of the Poisson's ratios, Young's moduli and shear moduli with the angle between the squares θ when the system is loaded in **a** Orientation I and **b** Orientation II. It is assumed that $k_s = 1$ and $z = 1$ (Grima et al. 2008). With kind permission from Springer Science+Business Media

The off-axis elastic moduli were also given by Grima et al. (2008) as

$$\nu_{12}^{\zeta} = -\frac{\cos^2(2\zeta)\sin\theta}{1+\sin^2(2\zeta)\sin\theta} \tag{2.5.21}$$

$$E_1^{\zeta} = -\frac{2k_s}{z\left[1+\sin^2(2\zeta)\sin\theta\right]} \tag{2.5.22}$$

$$G_{12}^{\zeta} = -\frac{k_s}{z[1+\cos(4\zeta)\sin\theta]} \tag{2.5.23}$$

where $\zeta = 0^\circ$ and $\zeta = 45^\circ$ correspond to Orientations I and II respectively. Figure 2.5.8 shows the off-axis elastic moduli plots.

In the case of auxetic behavior from rotating rectangles, as illustrated in Fig. 2.5.9(a), Grima et al. (2004) derived the following elastic properties

$$\nu_{21} = \frac{1}{\nu_{12}} = \frac{a^2\sin^2\left(\frac{\theta}{2}\right) - b^2\cos^2\left(\frac{\theta}{2}\right)}{a^2\cos^2\left(\frac{\theta}{2}\right) - b^2\sin^2\left(\frac{\theta}{2}\right)} \tag{2.5.24}$$

$$E_1 = 8K_h\frac{a\cos\left(\frac{\theta}{2}\right) + b\sin\left(\frac{\theta}{2}\right)}{\left[a\sin\left(\frac{\theta}{2}\right) + b\cos\left(\frac{\theta}{2}\right)\right]\left[-a\sin\left(\frac{\theta}{2}\right) + b\cos\left(\frac{\theta}{2}\right)\right]^2} \tag{2.5.25}$$

$$E_2 = 8K_h\frac{a\sin\left(\frac{\theta}{2}\right) + b\cos\left(\frac{\theta}{2}\right)}{\left[a\cos\left(\frac{\theta}{2}\right) + b\sin\left(\frac{\theta}{2}\right)\right]\left[a\cos\left(\frac{\theta}{2}\right) - b\sin\left(\frac{\theta}{2}\right)\right]^2} \tag{2.5.26}$$

based on the nomenclature furnished in Fig. 2.5.9b.

These property expressions are based on unit thickness, $z = 1$, and are reduced to the particular case of rotating square when $a = b = l$ is substituted into Eqs. (2.5.24)–(2.5.26), i.e. Equation (2.5.24) simplify to $\nu = -1$ when $a = b$ and both Eqs. (2.5.25) and (2.5.26) become Eq. (2.5.3) by substituting $a = b = l$ and $z = 1$. Figure 2.5.10 shows the variation of Poisson's ratio and the dimensionless Young's moduli for aspect ratio of $a/b = 2$ using Eqs. (2.5.24) to (2.5.26).

For the case of connected different-sized squares and rectangles, Grima et al. (2011) show that such systems can exhibit scale-independent auxetic behavior for stretching in particular directions, with Poisson's ratios being dependent on the shape and relative size of different rectangles in the model and the angle between them.

A real structure that exhibits similar mode of deformation was given by Taylor et al. (2013) for hole aspect ratio a/b that is sufficiently large and L_{min}/L_0 ratio that is sufficiently low, as shown in the simulated results (Fig. 2.5.11). Experimental validation on the finite element method (FEM) simulation's horizontal and vertical displacements has also been performed by Taylor et al. (2013) using digital image correlation (DIC), as shown in Fig. 2.5.12.

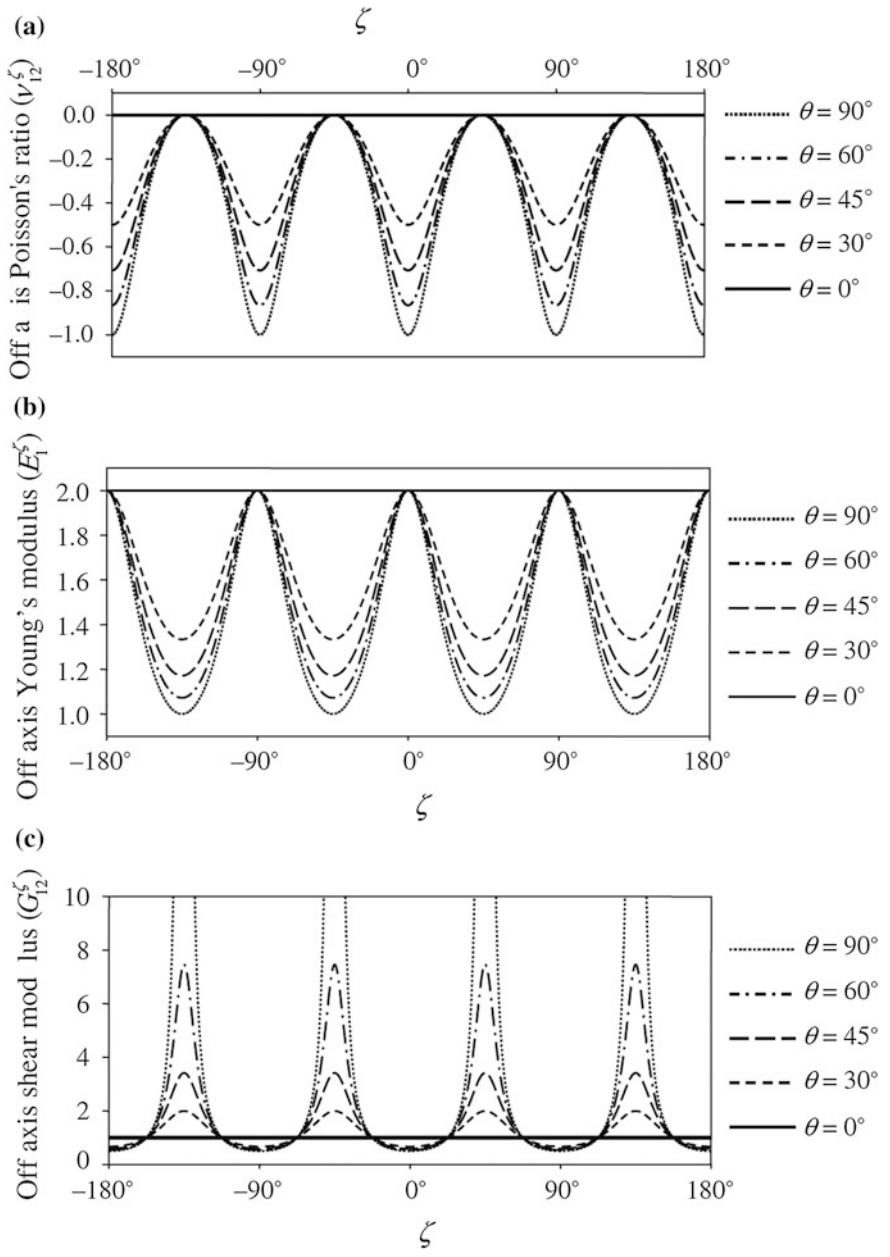

Fig. 2.5.8 Off-axis plots of **a** Poisson's ratio, **b** Young's modulus, and **c** shear modulus of the stretching mechanism at varying degrees of openness, assuming $k_s = 1$ and $z = 1$ (Grima et al. 2008). With kind permission from Springer Science+Business Media

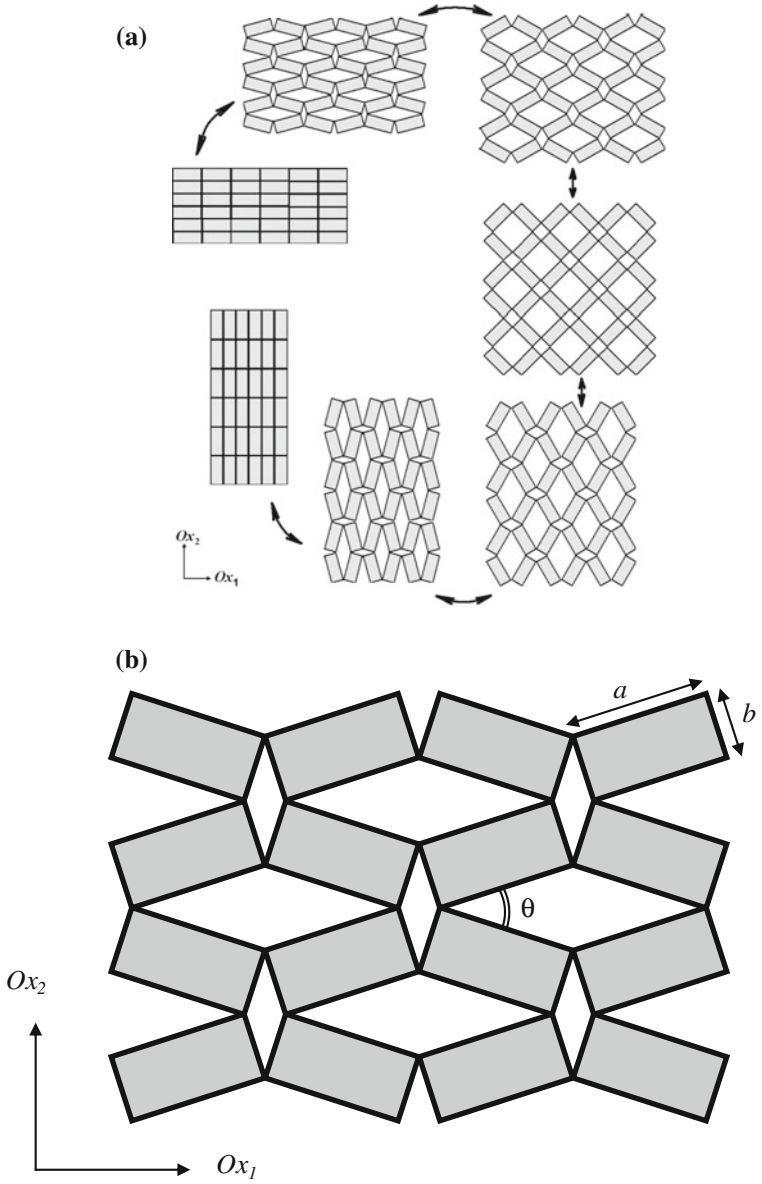

Fig. 2.5.9 **a** Auxetic behavior from *rotating rectangles*, and **b** dimensions adopted by Grima et al. (2004)

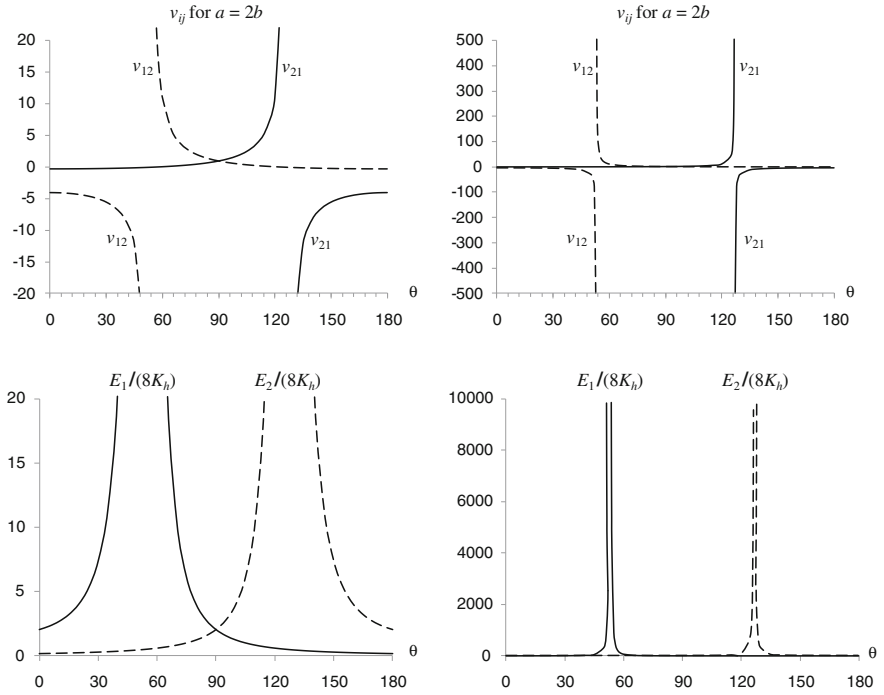

Fig. 2.5.10 Plots of Poisson's ratio (*top*) and Young's moduli (*bottom*) of *rotating rectangles* for unit thickness and aspect ratio of $a/b = 2$

2.6 Rotating Triangles Models

In addition to the rotating square model, Grima and Evans (2006) also pioneered the study on auxetic behavior using rotating triangles, as shown in Fig. 2.6.1a. Based on the schematics in Fig. 2.6.1b and adopting K_h and l as the rotational stiffness coefficient and length of the triangle side, respectively, Grima and Evans (2006) obtained the following elastic properties for rotating rigid triangles:

$$v_{12} = v_{21} = -1 \tag{2.6.1}$$

and

$$E_1 = E_2 = \frac{4\sqrt{3}\,K_h}{l^2}\left[1 + \cos\left(\frac{\pi}{3} + \theta\right)\right]^{-1}. \tag{2.6.2}$$

Sheets made from easily available conventional non-crystalline materials which contain star or triangular shaped perforations were simulated through FE models and were shown by Grima et al. (2010) to be capable of exhibiting auxetic behavior,

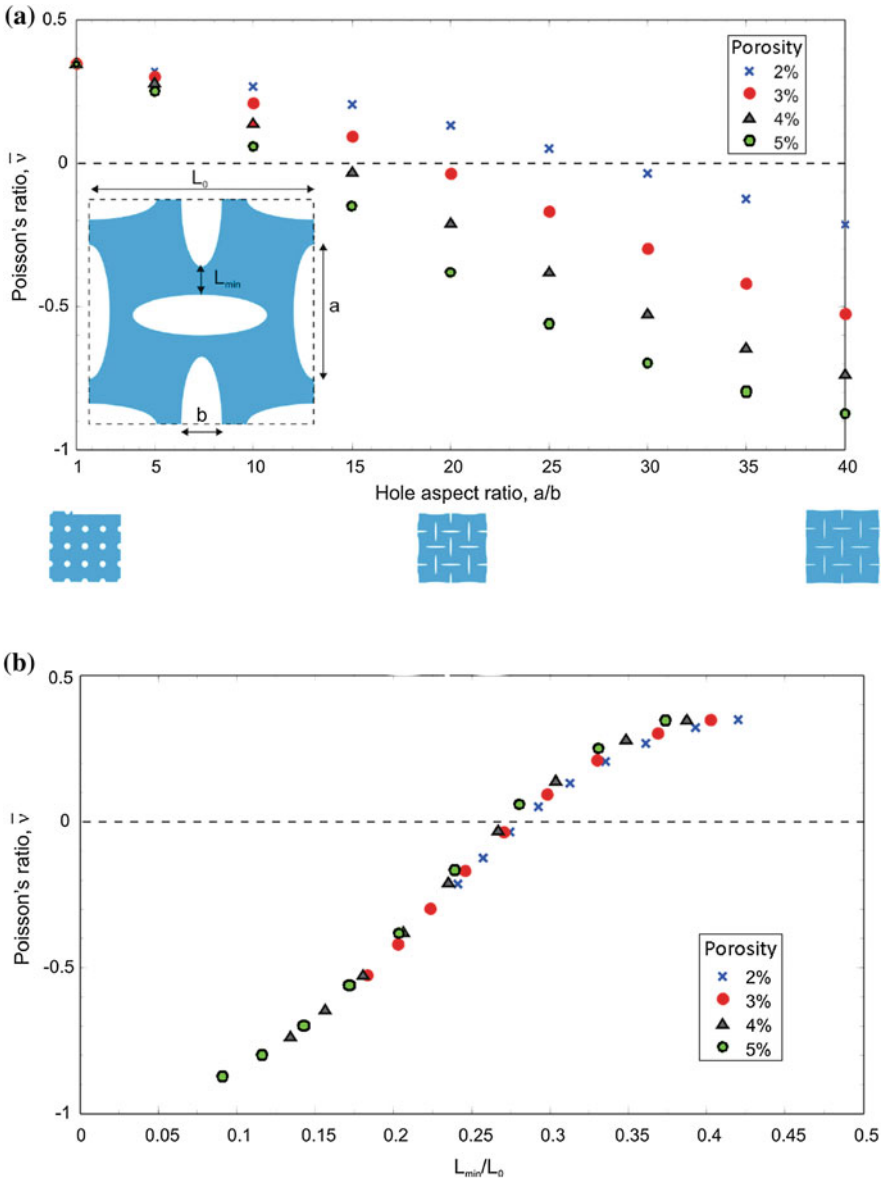

Fig. 2.5.11 **a** Results of the numerical investigation on the effect of the hole aspect ratio a/b for an infinite periodic square array in an elastic matrix. Four different values of porosity are considered. The RVE considered in the analysis is shown as an inset. **b** All data collapse on a single curve when the Poisson's ratio is plotted as a function of L_{min}/L_0 (Taylor et al. 2013). With kind permission from John Wiley & Sons

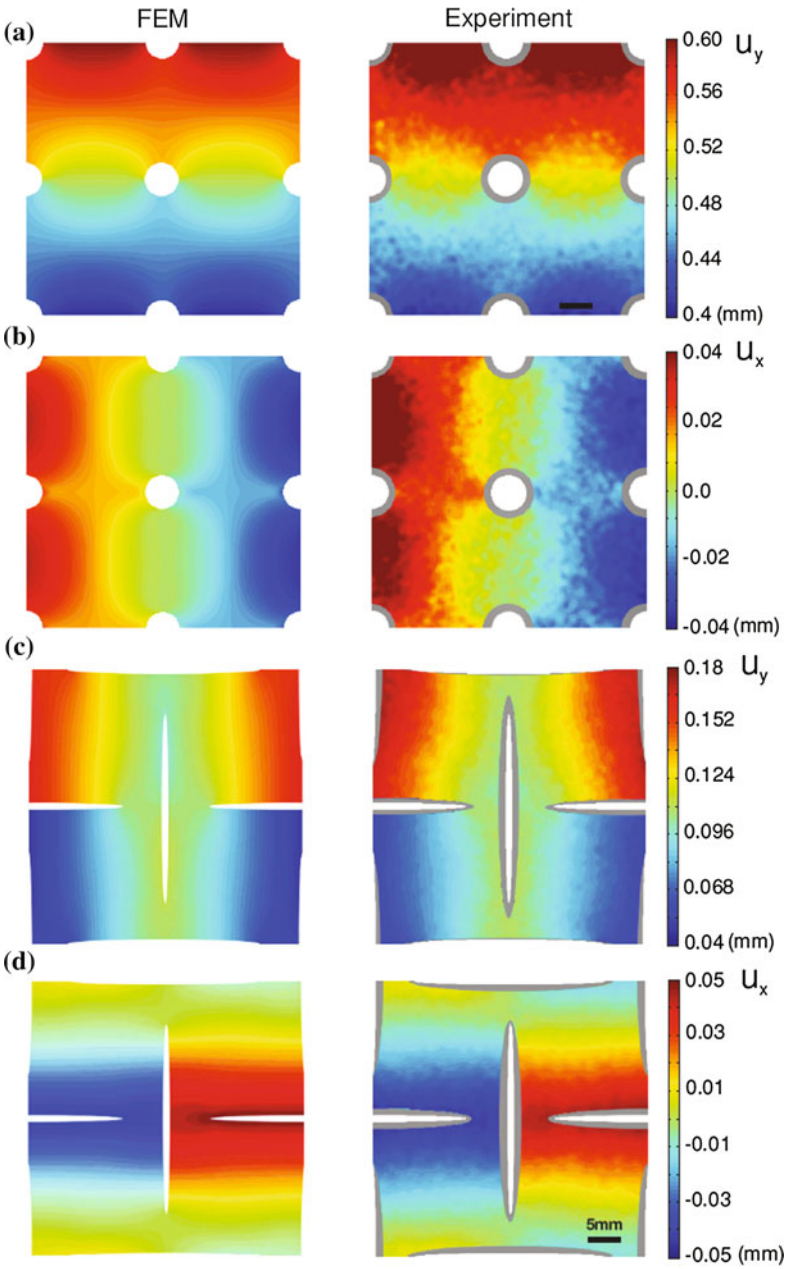

Fig. 2.5.12 Contour maps for the horizontal (u_x) and vertical (u_y) component of the displacement field. Numerical (*left*) and experimental (*right*) results are quantitatively compared, showing excellent agreement. In (**a**) and (**b**), the applied strain is 0.34 %, while in (**c**) and (**d**), the applied strain is 0.07 %. *Note* that gray areas on experimental results show regions where DIC data could not be obtained (Taylor et al. 2013). With kind permission from John Wiley & Sons

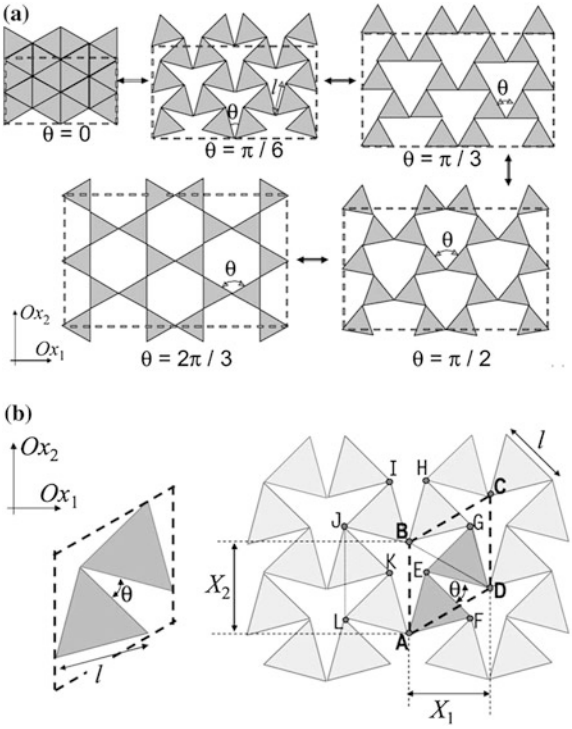

Fig. 2.6.1 a Auxetic behavior from rotating triangles, **b** definition of a typical repeat unit and unit cell (*left*) and definition of the geometric parameters (*right*) by Grima and Evans (2006). With kind permission from Springer Science+Business Media

a property which may be observed for loading in both tension and compression. An attempt was then made to explain this behavior in terms of analytical models based on "rotating rigid triangles" and they also showed that through careful choice of the shape and density of the perforations, one may control the magnitude and sign of the Poisson's ratio. This observation provides an easy and cost-effective method for the manufacture of systems at any scale which can be tailor made to exhibit particular values of the Poisson's ratio (auxetic or non-auxetic) so as to fit particular practical applications (Grima et al. 2010). A model based on scalene rigid triangles that rotate relative to one other was introduced and analyzed by Grima et al. (2012). It was demonstrated that this model can give a very wide range of Poisson's ratio values, the sign and magnitude of which depends on the shape of the triangles and the angles between them. An advantage of this model is that it is very generic and could possibly be employed for elucidating the behavior in various types of materials, such as auxetic foams and their relative surface density (Grima et al. 2012).

Chetcuti et al. (2014) proposed an extended model which not only allows for relative rotation of the units (joints), represented by non-equilateral triangular units, but also for differing amount of material at the joints as well as deformation of the joints themselves, a scenario that is more representative of real auxetic foams. This model shows that, by permitting deformation mechanisms other than rotation of the

triangles, the predicted extent of auxeticity decreases when compared to the equivalent idealized rotating rigid triangles model, thus resulting in more plausible predictions of the Poisson's ratios. Furthermore, Chetcuti et al. (2014) showed that in the manufacturing process, a minimum compression factor, which is dependent on the amount of materials at the joints, is required to obtain an auxetic foam from a conventional foam, as one normally observed in experimental work on foams.

2.7 Tetrahedral Framework Structure

A 3D version to the rotating squares, rectangles and triangles has been performed by Alderson and Evans (2001) in order to understand the auxetic properties of α-cristobalite via concurrent rotation and dilatation. The unit cell employed is tetragonal and contains four regular tetrahedron of uniform size, with edge length l, as depicted in Fig. 2.7.1a. The tetrahedra are connected at the corners such that in the extended network each corner is shared between two tetrahedral. Each tetrahedral is tilted about its tilt axis by an angle δ, as indicated in Fig. 2.7.1b, c, with

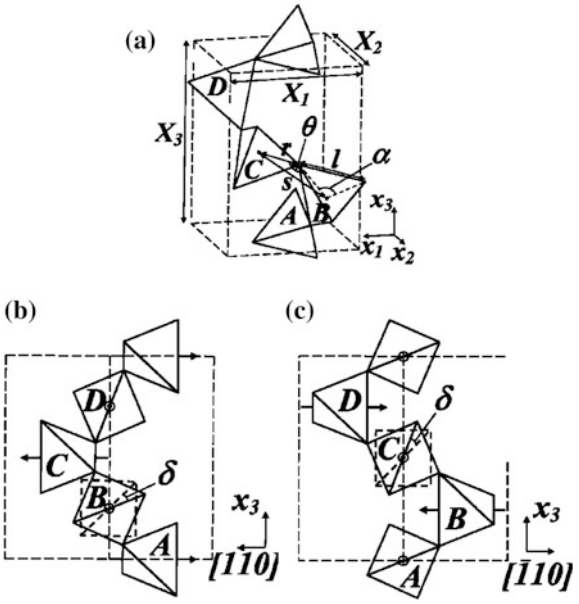

Fig. 2.7.1 **a** Unit cell for the tetrahedral framework by Alderson and Evans (2001), defining the geometrical parameters and coordinate system. The unit cell contains four tetrahedral: A, B, C and D. **b** x_3-[−110] projection of the unit cell, showing tetrahedral axes and "untilted" tetrahedron (B) to define tilt angle δ. **c** x_3-[−110] projection of the unit cell, showing tetrahedral axes and "untilted" tetrahedron (C) to define tilt angle δ (Alderson and Evans 2001). With kind permission from Springer Science+Business Media

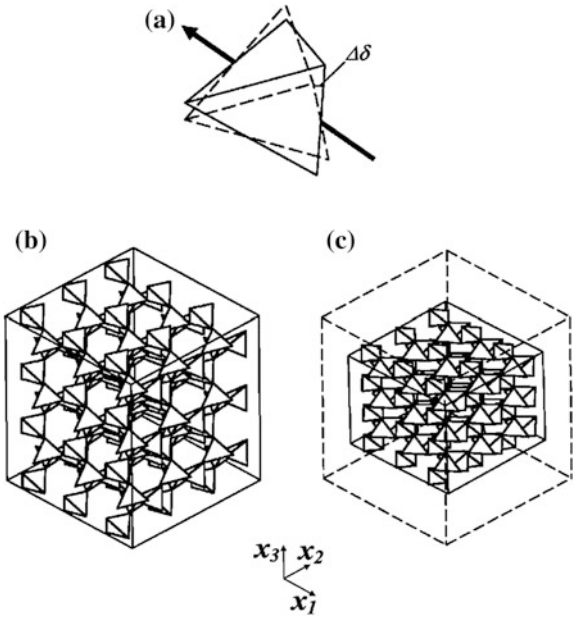

Fig. 2.7.2 Tetrahedra rotation mechanism. **a** Tetrahedral rotation about the tilt axis through the centers of two opposing tetrahedron edges. Tetrahedral size remains constant whereas tetrahedral orientation varies during rotation. **b** Fully expanded (i.e. $\delta = 0°$) 3 × 3 × 3 extended tetrahedral network. **c** Fully densified (i.e. $\delta = 45°$) 3 × 3 × 3 extended tetrahedral network (Alderson and Evans 2001). With kind permission from Springer Science+Business Media

$\delta = 0$ corresponding to the situation where the top and bottom edges of each tetrahedron are perpendicular to the x_3 axis.

In the rotating tetrahedral model (RTM), the tetrahedra are assumed to be rigid and free to rotate cooperatively around the tilt axis defining δ, whilst maintaining network connectivity, as shown in Fig. 2.7.2. In other words, the application of an external load results in a variation in δ (Alderson and Evans 2001). This mode of deformation is an extension of previous models, in which rigid SiO_4 tetrahedral rotation was used as a model for lattice parameter changes in silica structures undergoing phase transitions or thermal expansion.

In the second mode of deformation, which is termed the dilating tetrahedral model (DTM) by Alderson and Evans (2001), the tetrahedral are assumed to be fixed in orientation but free to deform by changing size (while maintaining tetrahedral regularity) in response to an applied load, i.e. l varies (Fig. 2.7.3). 2D analogies of this can be found in Rothenburg et al. (1991) and Milton (1992).

The third mode is a combination of RTM and DTM concurrently, hence the concurrent tetrahedral model (CTM). The Poisson's ratio v_{ij} for each mode was thus derived using the following constraints:

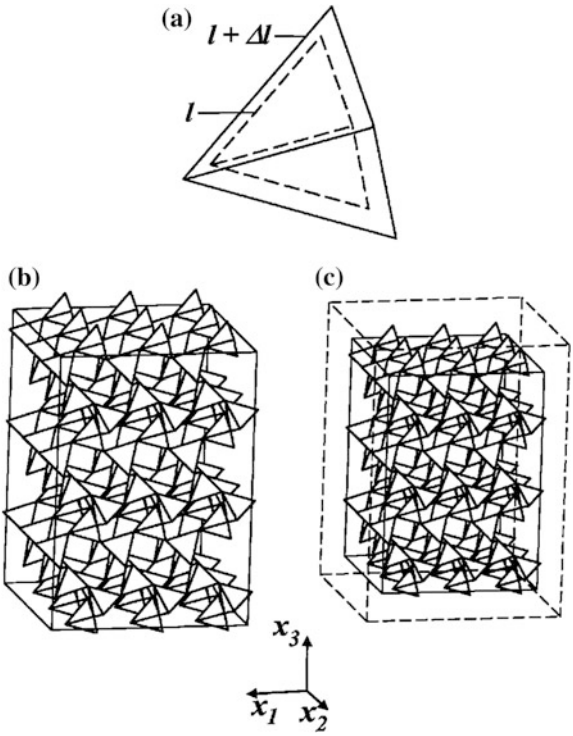

Fig. 2.7.3 Tetrahedra dilatation deformation mechanism. **a** Tetrahedral dilatation in which tetrahedral size varies whilst tetrahedral orientation remains constant during dilatation. **b** 3 × 3 × 3 extended tetrahedral network before tetrahedral dilatation. **c** 3 × 3 × 3 extended tetrahedral network after contraction of the tetrahedral, where δ has same value as (**b**) (Alderson and Evans 2001). With kind permission from Springer Science+Business Media

$$\text{RTM}: \ dl = 0 \tag{2.7.1}$$

$$\text{DTM}: d\delta = 0 \tag{2.7.2}$$

$$\text{CTM}: \ l\frac{d\delta}{dl} = \kappa \tag{2.7.3}$$

where κ is a weight parameter determining the relative strengths of the two concurrent deformation mechanisms. Alderson and Evans (2001) obtained

$$v_{12} = v_{21} = -1 \tag{2.7.4}$$

for DTM, RTM and hence also for CTM modes of deformation, while

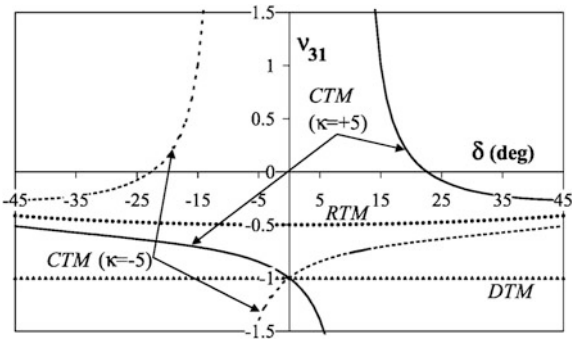

Fig. 2.7.4 v_{31} versus δ calculated from the RTM, DTM and CTM, with $-45° \leq \delta \leq 45°$. Curves for the CTM are shown for $\kappa = -5$ and $\kappa = 5$ (Alderson and Evans 2001). With kind permission from Springer Science+Business Media

$$v_{31} = -1 \tag{2.7.5}$$

based on the DTM mode of deformation,

$$v_{31} = -\frac{\cos\delta}{1+\cos\delta} \tag{2.7.6}$$

based on the RTM mode of deformation, and

$$v_{31} = -\frac{\cos\delta}{1+\cos\delta}\left(\frac{1+\cos\delta-\kappa\sin\delta}{\cos\delta-\kappa\sin\delta}\right) \tag{2.7.7}$$

for the CTM.

A particular feature of CTM is that there exists a range of κ values for any given value of δ for which positive values of v_{31} are realized, even though the two mechanisms in the model are each auxetic when acting independently, as shown in Fig. 2.7.4 (Alderson and Evans 2001).

2.8 Hard Cyclic Hexamers Model

The occurrence of negative Poisson's ratio in 2D system was suggested in the case of hard cyclic hexamers by Wojciechowski (1987) using Monte Carlo method. Wojciechowski (1987) commented that at high densities the molecules form a "tilted phase", whereby their centers of mass vibrate around sites of a hexagonal lattice and their axes librate around directions slightly rotated with reference to the crystal axes. See Fig. 2.8.1 for the definition of molecular axis, which joins the molecular center of mass and the point of contact between adjacent atoms.

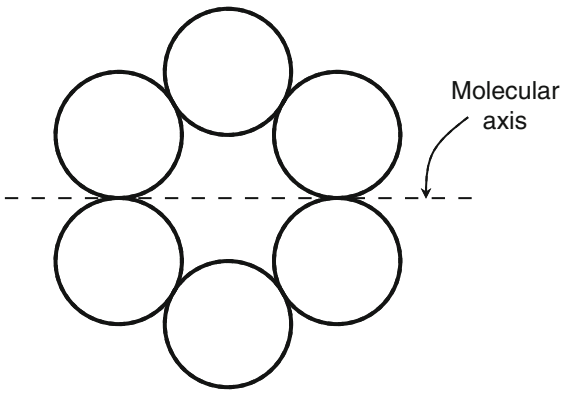

Fig. 2.8.1 Schematic diagram of a hard cyclic hexamer, with the molecular axis indicated

When the ratio of the actual area to the area of the system at close packing exceeds a particular value, the system transforms to the straight phase, i.e. the lattice of the centers of mass remains hexagonal but the mean directions of molecular axes are now oriented with the crystal axes. In addition to vibrational and librational motions these molecules also experience "jump-like" reorientations of about $\pi/3$ (Branka et al. 1982). Wojciechowski (1987) gave the following compliance:

$$S_{11} = \frac{C_{11}}{C_{11}^2 - C_{12}^2} = \frac{1}{16\lambda_1} + \frac{1}{8\lambda_2} \tag{2.8.1}$$

$$S_{12} = -\frac{C_{11}}{C_{11}^2 - C_{12}^2} = \frac{1}{16\lambda_1} - \frac{1}{8\lambda_2} \tag{2.8.2}$$

$$S_{66} = \frac{1}{C_{66}} = \frac{1}{2\lambda_2} \tag{2.8.3}$$

in which the quantities λ_1 and λ_2 can be calculated upon experimental measurement of C_{11} and C_{66}. It is known the following compliance

$$S_{12} = S_{11} - \frac{1}{2}S_{66} \tag{2.8.4}$$

typically possesses negative values, thereby indicating positive Poisson's ratio. Hence Wojciechowski (1987) discovered an auxetic case in which S_{12} is a positive value for the tilted phase. Wojciechowski (1989) then studied a 2D lattice model of hexagonal molecules on a triangular lattice interacting through a nearest-neighbor n-inverse-power site-site potential, which reveals negative Poisson ratio at high densities when the anisotropy non-convexity of the molecules is substantial, and proposed that such a behavior could be observed in some real systems. In a related investigation using a simple free-volume (FV) approximation, Wojciechowski and Branka (1989) examined a 2D system of hard cyclic hexamers with negative

Poisson ratio in a high-density crystalline phase, in which the FV approximation and a lattice model indicate the crucial role of broken mirror symmetry for the observed auxeticity.

2.9 Missing Rib Models

A missing rib model was proposed by Smith et al. (2000) for modeling the elastic properties of auxetic foams. The missing rib model is called as such because its idealized microstructure is derived from the intact model (which is conventional) and the removal of some ribs leads to the cut version, or the missing rib model, which is auxetic. See Fig. 2.9.1 (top). With reference to the Fig. 2.9.1 (bottom left), Smith et al. (2000) obtained the following elastic moduli

$$v_{21} = \frac{1}{v_{12}} = \tan^2\left(\frac{\zeta}{2}\right) \tag{2.9.1}$$

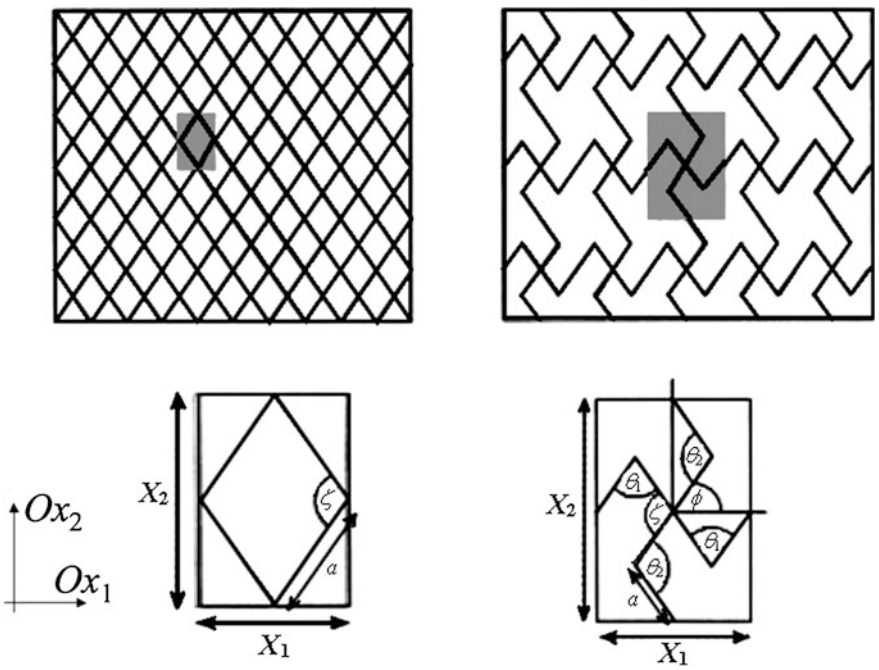

Fig. 2.9.1 The idealized networks of the intact version (*top left*) and the cur version (*top right*) with the unit cells shaded, as well as the unit cells chosen for the intact version (*bottom left*) and cut version (*bottom right*) along with their geometrical parameters (Smith et al. 2000). With kind permission from Elsevier

$$E_1 = \frac{4k_\zeta}{a^2}\cot\left(\frac{\zeta}{2}\right)\csc^2\left(\frac{\zeta}{2}\right) \tag{2.9.2}$$

$$E_2 = \frac{4k_\zeta}{a^2}\tan\left(\frac{\zeta}{2}\right)\sec^2\left(\frac{\zeta}{2}\right) \tag{2.9.3}$$

for the intact model, where k_ζ is the spring constant that restraints the change to the angle ζ.

With reference to Fig. 2.9.1 (bottom right), Smith et al. (2000) obtained the following elastic moduli

$$\nu_{21} = \frac{1}{\nu_{12}} = -\tan(\phi)\tan(\zeta - \phi) \tag{2.9.4}$$

$$E_1 = \frac{k_\theta}{4a^2}\frac{\cot(\zeta - \phi)}{\sin(\phi)\sin(\zeta - \phi)} \tag{2.9.5}$$

$$E_2 = \frac{k_\theta}{4a^2}\frac{\tan(\zeta - \phi)}{\cos(\phi)\cos(\zeta - \phi)} \tag{2.9.6}$$

for the missing rib model, where k_θ is the spring constant that restrains the change to the angle θ.

A Poisson's ratio function comparison between the hexagonal model, as described in Eq. (2.2.1) for both conventional and auxetic foams with the intact model, as well as the intact and missing rib models, as described by Eqs. (2.9.1) and (2.9.4) respectively, with experimental results is shown in Fig. 2.9.2. The values of θ in the hexagonal model are obtained when fitted to the conventional and auxetic foams, as furnished in Table 2.9.1.

The true stress versus true strain behavior of both the honeycomb and the rib model by Smith et al. (2000) are shown in Fig. 2.9.3 using the best fit predictions.

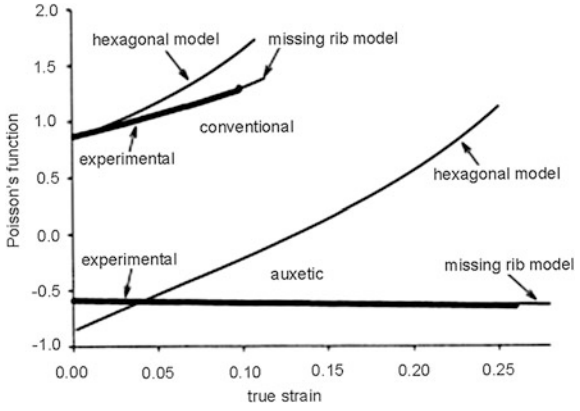

Fig. 2.9.2 Poisson's function and the true strain data of the foam specimens by Smith et al. (2000). With kind permission from Elsevier

Table 2.9.1 Values of the parameters used to calculate the Poisson's function data in Fig. 2.9.2 for the hexagonal array honeycomb (hexagonal shape for conventional and re-entrant shape for auxetic foams), as well as the intact and missing rib models for the conventional and re-entrant foams respectively by Smith et al. (2000)

Honeycomb array	Hexagonal shape (conventional)	Re-entrant shape (auxetic)
h	2	2
l	1	1
θ	19.2°	−25.99°
k	0.03	0.03
Rib model by Smith et al. (2000)	Intact model or rhombus unit cell (conventional)	Missing rib model or swastika unit cell (auxetic)
a	1	1
ζ	85.7	77.3°
ϕ	–	24.1°
θ_1 and θ_2	–	73.4° and 48.1°
k_θ or k_ζ	$k_\zeta = 0.01429$	$k_\theta = 0.08333$

With kind permission from Elsevier

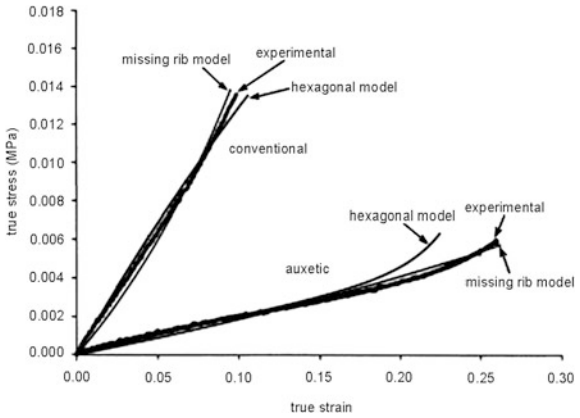

Fig. 2.9.3 True stress versus true strain of experimental data and theoretical predictions by the honeycomb and the rib models by Smith et al. (2000). With kind permission from Elsevier

The conventional foam possesses a higher Young's modulus as expected. More importantly, Smith et al. (2000) noted that the traditional 2D honeycomb model by Masters and Evans (1996) is valid for describing the strain-dependent behavior of conventional foams but not for auxetic ones; i.e. the missing rib model caters to the realistic cell geometries.

Following up on this work, Gaspar et al. (2005) compared the behavior of two conventional and two auxetic honeycomb structures, as shown in Fig. 2.9.4(a). Based on the test procedure shown in Fig. 2.9.4(b), Gaspar et al. (2005) obtained a set of experimental data for the measured angles of ζ and ϕ, as shown in Fig. 2.9.4 (d). Plots of the Poisson's ratio versus strain in the loading direction are shown in Fig. 2.9.4(c).

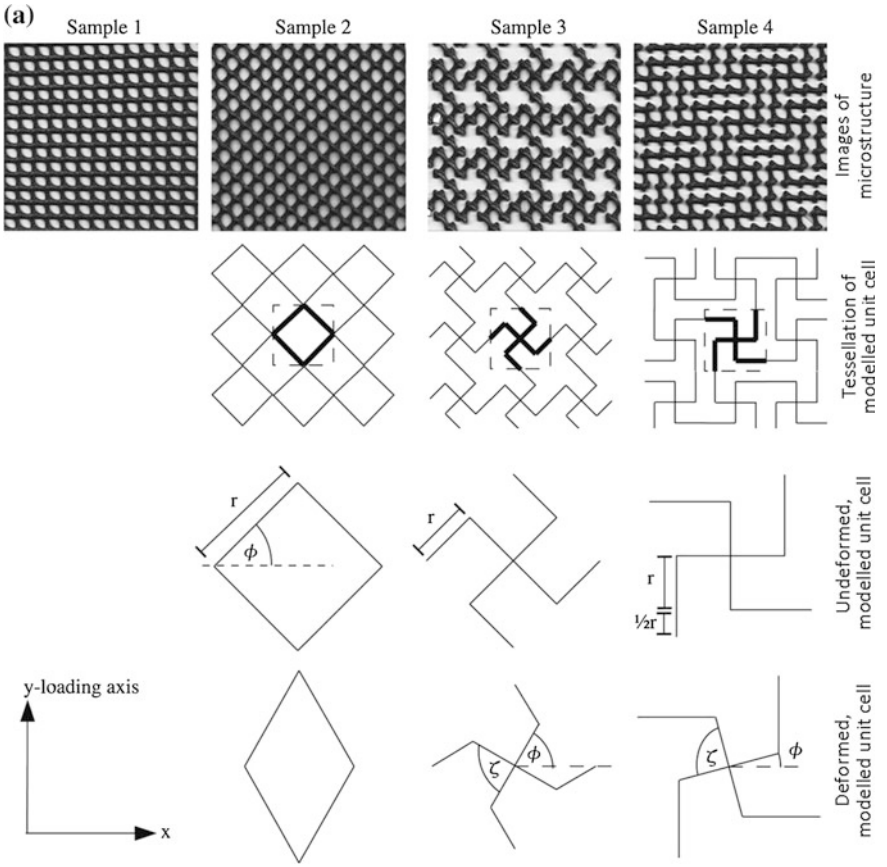

Fig. 2.9.4 **a** Conventional and missing rib foams, **b** diagram for test method, **c** measured Poisson's ratio, and **d** mean measured angles, where TC is the total change in the value between the initial and the final strain point and the standard deviation (SD) is taken at the final strain point over 20 cells (Gaspar et al. 2005). With kind permission from Elsevier

An alternate missing rib model was introduced by Lim et al. (2014) upon observing photomicroscopy of both the conventional and auxetic materials using light microscopy, as shown in Fig. 2.9.5. It could be clearly seen that the conventional foam resembles hexagonal microstructures, while the auxetic foam did not give a clear view. In order provide a clearer view, thin slices of both foam materials were made and viewed under coarse microscopy. Figure 2.9.6a clearly shows again that the assumption of hexagonal microstructure is quite valid. However, no clear indication can be seen for the case of auxetic foams. Thereafter a finer imaging using light microscopy was made, with startling results.

As shown in Fig. 2.9.6b, the assumption of re-entrant structure that is commonly adopted for modeling auxetic materials is invalid. Rather, the microscopy image shows that there is high level of irregularity in the microstructure in both the shape

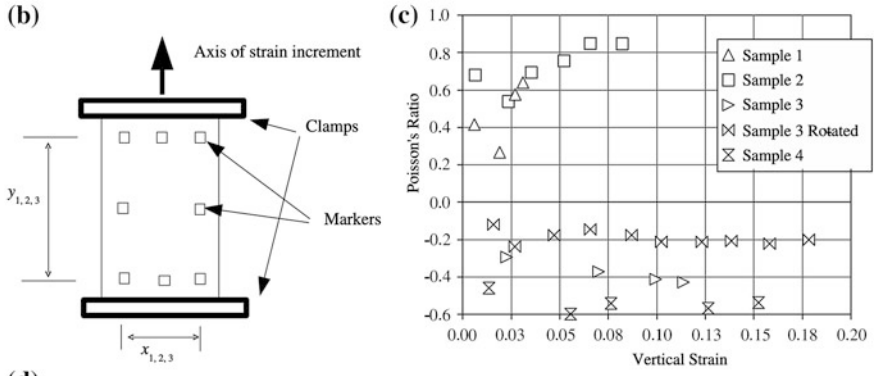

(d)

Sample	Angle	Angle data point											TC	SD
		0	1	2	3	4	5	6	7	8	9	10		
2	ϕ	43.0	43.5	44.5	45.1	46.1	47.2	47.8					4.8	1.1
3	ζ	91.8	93.1	94.0	96.1	97.0							5.1	2.3
	ϕ	48.5	50.8	52.4	56.1	56.2							7.7	2.7
3	ζ	88.7	88.6	66.3	88.6	88.7	89.5	90.6	91.3	91.6	92.6	92.9	4.1	1.8
90°	ϕ	44.5	44.5	45.4	45.9	47.2	49.4	48.7	52.0	52.0	54.3	53.7	9.2	1.0
4	ζ	91.2	91.4	92.9	93.1	94.6	96.8						5.6	6.1
	ϕ	0.4	5.4	10.0	12.1	17.3	21.3						21.0	4.5

Fig. 2.9.4 (continued)

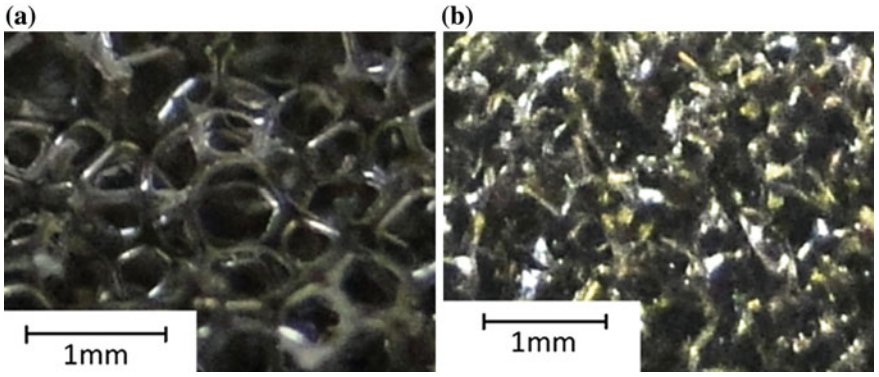

Fig. 2.9.5 Microphotography of PU foam specimens: **a** conventional, and **b** auxetic by Lim et al. (2014). With kind permission from John Wiley & Sons

and size. Consideration of Figs. 2.9.5 and 2.9.6 shows that the individual cells in conventional foams are convex from the outside or concave from the inside, while both concave and convex surfaces are found on both sides of individual cell's wall

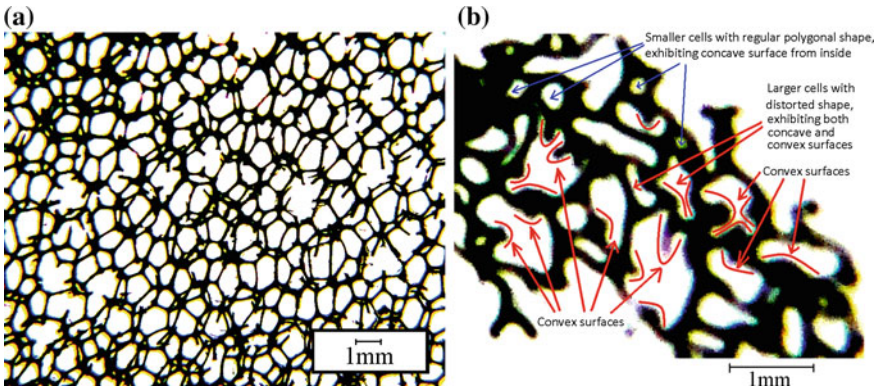

Fig. 2.9.6 Microphotography from thin slices of PU foams: **a** conventional specimen, and **b** auxetic specimen. With kind permission from John Wiley & Sons

in the case of auxetic foams. Furthermore the individual cells are of similar sizes for conventional foams but very different in the case of auxetic foams.

Based on these two observations, a possible model is proposed for auxetic foams by means of missing rib from hexagonal cellular structure, as shown in Fig. 2.9.7. Unlike the cells in Fig. 2.9.6a, which are all almost about the same size, the cells in Fig. 2.9.6b are of different sizes. As such, the model displayed in Fig. 2.9.7 allows the RVE to be represented both by larger and smaller cells, as inspired by Fig. 2.9.6b and the works by Pozniak et al. (2013).

The experimentally studied foams are isotropic at macro level, which is a consequence of their disordered structure. The model considered is highly ordered as its structure is periodic. It is well known that 6-fold axis implies isotropic elastic

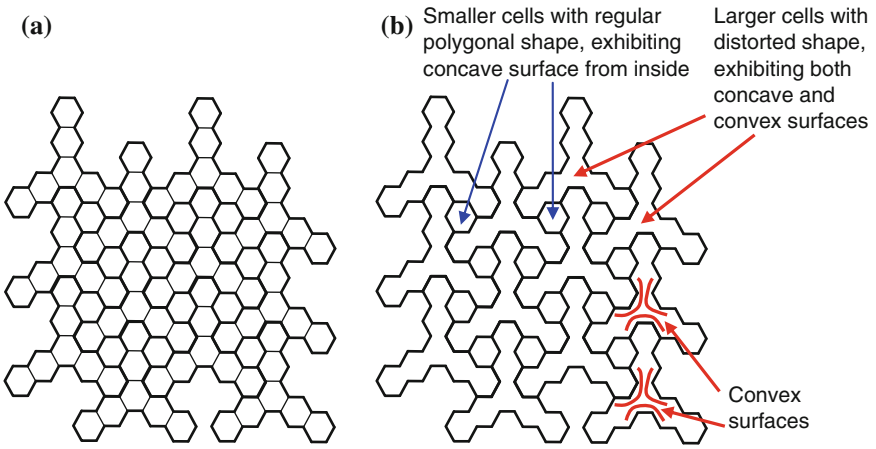

Fig. 2.9.7 Hexagonal-based missing rib model for describing auxetic foams: **a** before rib deletion (ribs to be removed are denoted as *thin lines*), and **b** after rib deletion by Lim et al. (2014). With kind permission from John Wiley & Sons

properties in planes perpendicular to the axis but the studied structure does not exhibit 6-fold symmetry by a lower, 3-fold symmetry axis. The fact that this is a sufficient symmetry to obtain planar isotropy has been pointed out by Wojciechowski (2003). Typical foams are strongly disordered but nevertheless isotropic. Although the proposed model is perfectly ordered, its rotation-based deformation allows isotropic auxetic characteristics to be manifested.

In this model, the relative difference between the small and large cell sizes is comparable to those shown in Fig. 2.9.6(b), in which the smaller cells generally exhibit regular polygonal shapes while the larger cells exhibit more distorted shapes. In addition, this model allows auxetic behavior to be exhibited by means of rotation. It is possible to compare this missing rib model with the missing rib model proposed by Smith et al. (2000) for describing auxetic behavior in reticulated foams, which is based on the a network of ribs with biaxial symmetry that exhibits rhombus cells, such that the removal of a proportion of the cell ribs leads to swastika network that manifests auxetic property via rotation mechanism. The proposed model by Lim et al. (2014) is based on hexagonal cells such that the removal of a proportion of the cell ribs leads to both large distorted cells and small regular-shaped cells to exhibit auxetic behavior by means of rotation, and at the same time partially reflect the foam microstructural geometry.

With reference to Fig. 2.9.8a for an RVE, the small cells are surrounded by foam walls on all six sides, and are therefore of comparatively high stiffness. The center of the RVE is a highly "open" partial cell, which is surrounded by only three walls, thereby allowing greater deformation. The remaining hexagons are filled with partial cells that are surrounded by four or five walls, and are therefore of moderate stiffness. The surrounding regions of high, moderate and low stiffness are shown in Fig. 2.9.8b. For this missing rib model, the rigidity of the high stiffness region, denoted by "H", avails its function as a rotating unit. The rotation of the

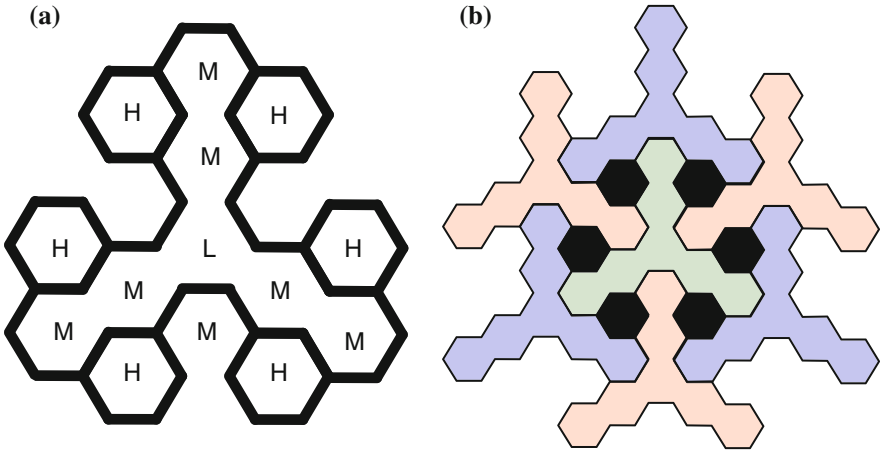

Fig. 2.9.8 The proposed model showing: **a** an RVE with regions of high stiffness (*H*), moderate stiffness (*M*) and low stiffness (*L*), and **b** a central RVE surrounded by six other RVEs, with the rotating cells shaded in *black* (Lim et al. 2014). With kind permission from John Wiley & Sons

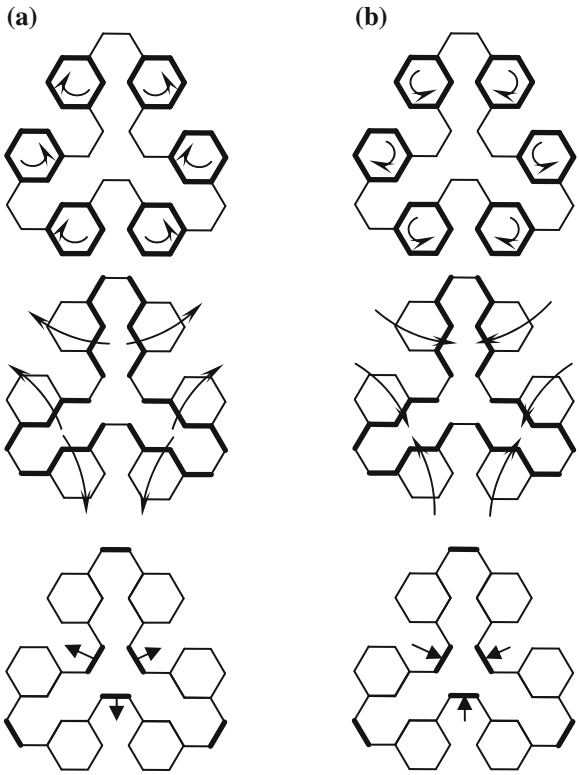

Fig. 2.9.9 Iso-expansion (**a**) and iso-contraction (**b**) for the missing rib model by Lim et al. (2014). With kind permission from John Wiley & Sons

comparatively rigid units leads to the collapse or expansion of the low stiffness region, denoted by "L". Figure 2.9.9a, b shows how the direction of rotation of the H regions opens or closes the L regions, leading to 2-dimensional iso-expansion and iso-contraction respectively.

2.10 Chiral and Anti-chiral Lattice Models

Another model that gives rise to auxetic behavior is the chiral lattice model. In this model, each rigid ring is connected by six ligaments that are attached in a tangential fashion, as illustrated in Fig. 2.10.1. It can be easily seen from this model that tensile loading in one direction causes the elongation in the direction of loading by means of clockwise rotation of the rigid rings. The ring rotation consequently enlarges the entire network, thereby leading to an in-plane auxetic property.

A theoretical and experimental investigation was conducted of a two-dimensionally chiral honeycomb by Prall and Lakes (1997), in which the honeycomb exhibits a Poisson's ratio of $\nu = -1$ for in-plane deformation. This Poisson's ratio is maintained over a significant range of strain, in contrast to the variation with strain seen in known

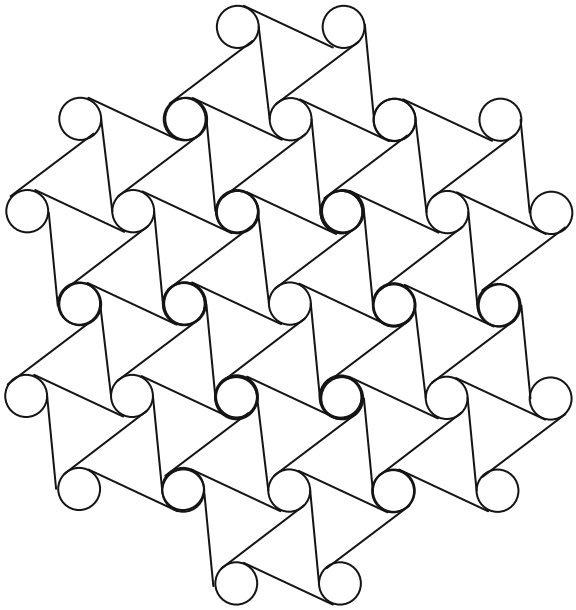

Fig. 2.10.1 Auxetic behavior from chiral lattice in hexagonal array

negative Poisson's ratio materials. The ligament is modeled as beam of thickness t and length L, while the ring has a radius r (Fig. 2.10.2). For a base material of Young's modulus E_s, Prall and Lakes (1997) gave the in-plane Young's modulus as

$$E = \sqrt{3}E_s\left(\frac{L}{r}\right)^2\left(\frac{t}{L}\right)^3 \tag{2.10.1}$$

in which a similar dependence on $(t/L)^3$ is found for the honeycomb model by Gibson and Ashby (1988).

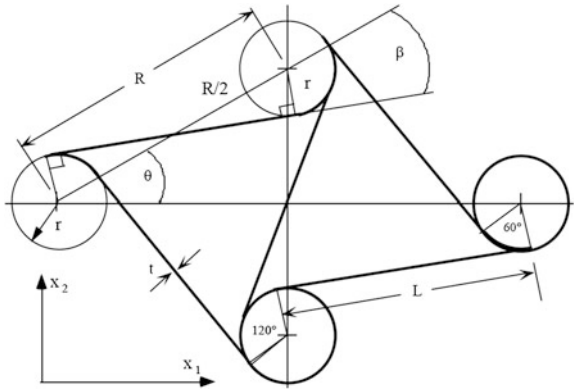

Fig. 2.10.2 Geometry for analysis of chiral lattice by Prall and Lakes (1997). With kind permission from Elsevier

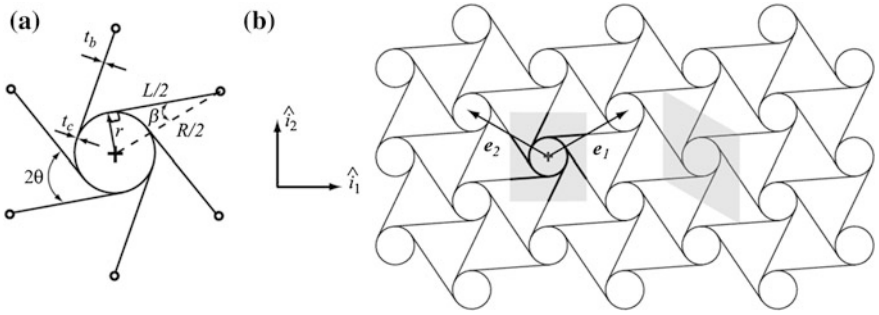

Fig. 2.10.3 Geometry of a hexagonal chiral lattice: **a** unit cell and **b** unit volume with symmetry vectors. With kind permission from Elsevier

A chiral lattice investigated with an equivalent, micropolar-continuum model was attempted to remove the indeterminacy $\nu = -1$ encountered by Prall and Lakes (1997) and Spadoni et al. (2009). Based on the geometry nomenclature laid out in Fig. 2.10.3, Spadoni and Ruzzene (2012) developed constitutive models for two cases. In the first case the nodes are assumed rigid while in the second case the nodes are allowed to deform. The constitutive relation for the rigid node case was developed analytically while the constitutive relation for the deformable node case was developed numerically via a finite element model.

For the case of rigid nodes, Spadoni and Ruzzene (2012) obtained the constitutive relation

$$\begin{Bmatrix} \sigma_{11} \\ \sigma_{22} \\ \sigma_{12} \\ \sigma_{21} \\ m_{13} \\ m_{23} \end{Bmatrix} = \begin{bmatrix} D_{11} & D_{12} & 0 & 0 & 0 & 0 \\ D_{21} & D_{22} & 0 & 0 & 0 & 0 \\ 0 & 0 & D_{33} & D_{34} & 0 & 0 \\ 0 & 0 & D_{43} & D_{44} & 0 & 0 \\ 0 & 0 & 0 & 0 & D_{55} & 0 \\ 0 & 0 & 0 & 0 & 0 & D_{66} \end{bmatrix} \begin{Bmatrix} \varepsilon_{11} \\ \varepsilon_{22} \\ \varepsilon_{12} \\ \varepsilon_{21} \\ \kappa_{13} \\ \kappa_{23} \end{Bmatrix} \tag{2.10.2}$$

where

$$D_{11} = D_{22} = \frac{\sqrt{3}E_s t}{4L^3} \frac{(t^4 - L^4)\cos^2\beta + L^4 + 3L^2t^2}{(t^2 - L^2)\cos^2\beta + L^2} \tag{2.10.3}$$

$$D_{12} = D_{21} = -\frac{\sqrt{3}E_s t}{4L^3} \frac{L^4\tan^2\beta + t^4 - L^2t^2(1 + \tan^2\beta)}{L^2\tan^2\beta + t^2} \tag{2.10.4}$$

$$D_{33} = D_{44} = \frac{\sqrt{3}E_s t}{4L^3} \frac{2L^4\tan^2\beta + L^2R^2 + t^2(2L^2 + R^2)}{R^2} \tag{2.10.5}$$

$$D_{34} = D_{43} = -\frac{\sqrt{3}E_s t}{4L^3}\frac{2L^4\tan^2\beta - L^2R^2 + t^2(2L^2 - R^2)}{R^2} \tag{2.10.6}$$

$$D_{55} = D_{66} = \frac{\sqrt{3}E_s t}{4L^3}\left(L^4\tan^2\beta + \frac{4}{3}L^2t^2\right). \tag{2.10.7}$$

Using the treatments of Nakamura and Lakes (1995) and Yang and Huang (2001), the engineering constants in terms of stiffness coefficients $E = (D_{11}^2 - D_{12}^2)/D_{11}$ and $v = D_{12}/D_{11}$ were expressed by Spadoni and Ruzzene (2012) as

$$E = \frac{2\sqrt{3}\left[1 + \left(\frac{t}{L}\right)^2\right]\left(\frac{t}{L}\right)^3}{\left(\frac{t}{L}\right)^4\cos^2\beta + \sin^2\beta + 3\left(\frac{t}{L}\right)^2}E_s \tag{2.10.8}$$

$$v = \frac{4\left(\frac{t}{L}\right)^2}{\left(\frac{t}{L}\right)^4\cos^2\beta + \sin^2\beta + 3\left(\frac{t}{L}\right)^2} - 1 \tag{2.10.9}$$

$$G = \frac{\sqrt{3}}{4}\frac{t}{L}\left[1 + \left(\frac{t}{L}\right)^2\right]E_s. \tag{2.10.10}$$

Due to the complexity in obtaining analytical expressions for the case of deformable rings, Spadoni and Ruzzene (2012) adopted FE model with the imposed displacements and rotations to the corresponding strain states as shown in Fig. 2.10.4. Results of the Young's modulus, shear modulus and Poisson's ratio for both the case of rigid node by analytical approach and the case of deformable node by the finite element approach are shown in Fig. 2.10.5, whereby the Young's and shear moduli were plotted in normalized forms, i.e. $\overline{E}_m/(t/L)^3$ and $\overline{G}_m/(t/L)^3$ respectively, in which

$$\begin{Bmatrix} \overline{E}_m \\ \overline{G}_m \end{Bmatrix} = \frac{1}{E_s}\begin{Bmatrix} E \\ G \end{Bmatrix}. \tag{2.10.11}$$

In relation to this chiral lattice, the auxeticity of chiral and anti-chiral lattices, such as those shown in Fig. 2.10.6, have also been studied by Alderson et al. (2010b). Other investigations on chiral and anti-chiral models have been performed by Alderson et al. (2010a), Miller et al. (2010), Lorato et al. (2010), Michelis and Spitas (2010), Abramovitch et al. (2010), Kopyt et al. (2010).

The anti-tetrachiral structure model by Chen et al. (2013) was investigated analytically and by finite element approach. Based on the structure shown in Fig. 2.10.7, Chen et al. (2013) established the following elastic moduli:

$$v_{xy} = -\frac{L_x}{L_y} \tag{2.10.12}$$

(a)

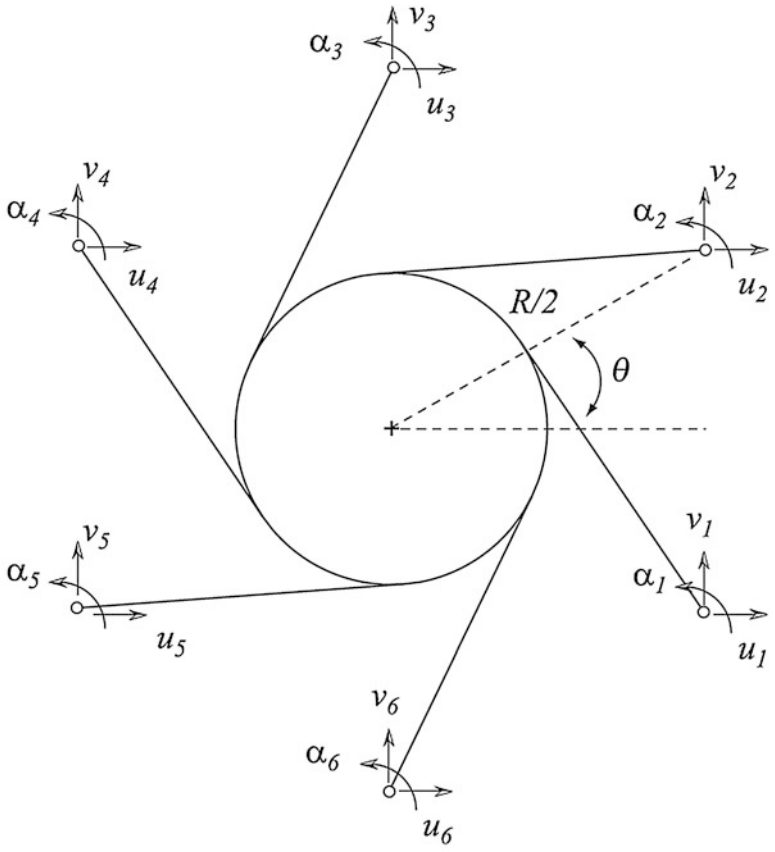

(b)

	ε_{11}	ε_{22}	ε_{12}	ε_{21}	κ_{13}	κ_{23}
u_1	$R\cos\theta/2$	0	$-R\sin\theta/2$	0	0	0
v_1	0	$-R\sin\theta/2$	0	$R\cos\theta/2$	0	0
α_1	$\hat{\alpha}_1$	$\hat{\alpha}_1$	$\hat{\alpha}_1+1/2$	$\hat{\alpha}_1-1/2$	$R\cos\theta/2$	$-R\sin\theta/2$
u_2	$R\cos\theta/2$	0	$R\sin\theta/2$	0	0	0
v_2	0	$R\sin\theta/2$	0	$R\cos\theta/2$	0	0
α_2	$\hat{\alpha}_2$	$\hat{\alpha}_2$	$\hat{\alpha}_2+1/2$	$\hat{\alpha}_2-1/2$	$R\cos\theta/2$	$R\sin\theta/2$
u_3	0	0	$R/2$	0	0	0
v_3	0	$R/2$	0	0	0	0
α_3	$\hat{\alpha}_3$	$\hat{\alpha}_3$	$\hat{\alpha}_3+1/2$	$\hat{\alpha}_3-1/2$	0	$R/2$

Fig. 2.10.4 **a** FE model of the unit cell employed to study configurations with deformable rings with boundary degrees of freedom prescribed for each considered strain state, and **b** imposed displacements corresponding to six independent strain states (Spadoni and Ruzzene 2012). With kind permission from Elsevier

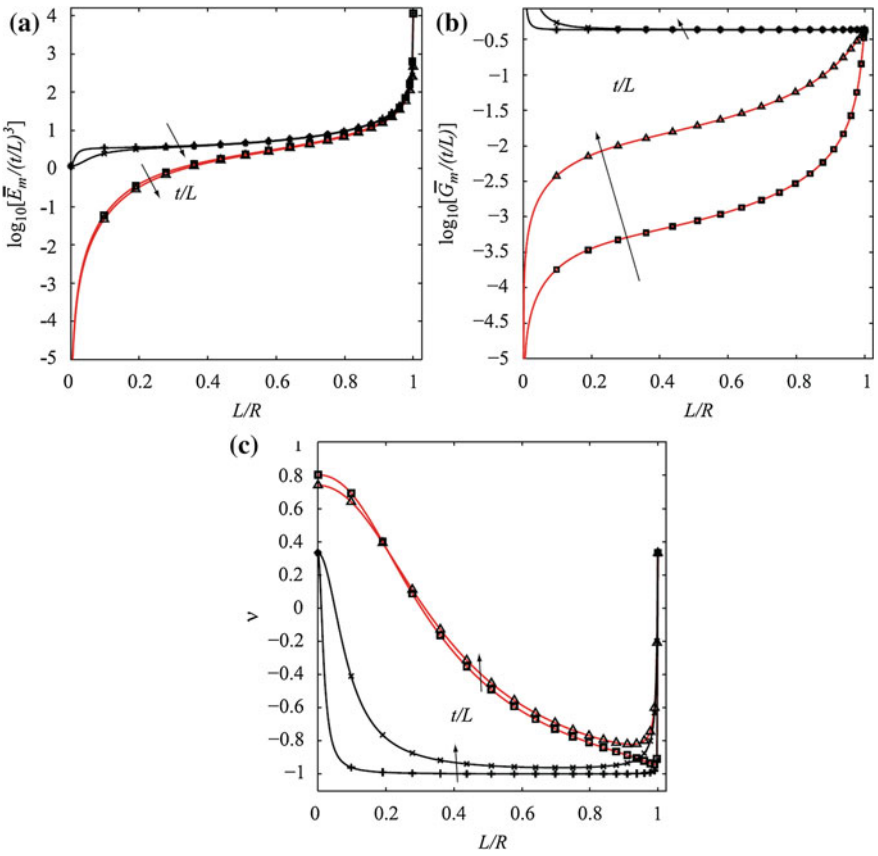

Fig. 2.10.5 Micropolar engineering constants for the chiral lattice with two values of ligament aspect ratio t/L = 1/100, 1/20 with rigid rings (*plus* and *multiplication* symbols) and deformable rings (*square* and *triangle* symbols) rings. Normalized **a** Young's modulus, **b** shear modulus, and **c** Poisson's ratio (Spadoni and Ruzzene 2012). With kind permission from Elsevier

$$E_x = \frac{E_c \beta^3 \alpha_x}{12(1-\beta/2)^2 \alpha_y} \left(\frac{1}{\alpha_x - 2\sqrt{2\beta - \beta^2}} + \frac{1}{\alpha_y - 2\sqrt{2\beta - \beta^2}} \right) \tag{2.10.13}$$

$$E_y = \frac{E_c \beta^3 \alpha_y}{12(1-\beta/2)^2 \alpha_x} \left(\frac{1}{\alpha_x - 2\sqrt{2\beta - \beta^2}} + \frac{1}{\alpha_y - 2\sqrt{2\beta - \beta^2}} \right) \tag{2.10.14}$$

$$E_z = \frac{\beta\left[\alpha_x + \alpha_y + \pi(2-\beta)\right] - 2[\phi - (1-\beta)\sin\phi]}{\alpha_x \alpha_y} E_c \tag{2.10.15}$$

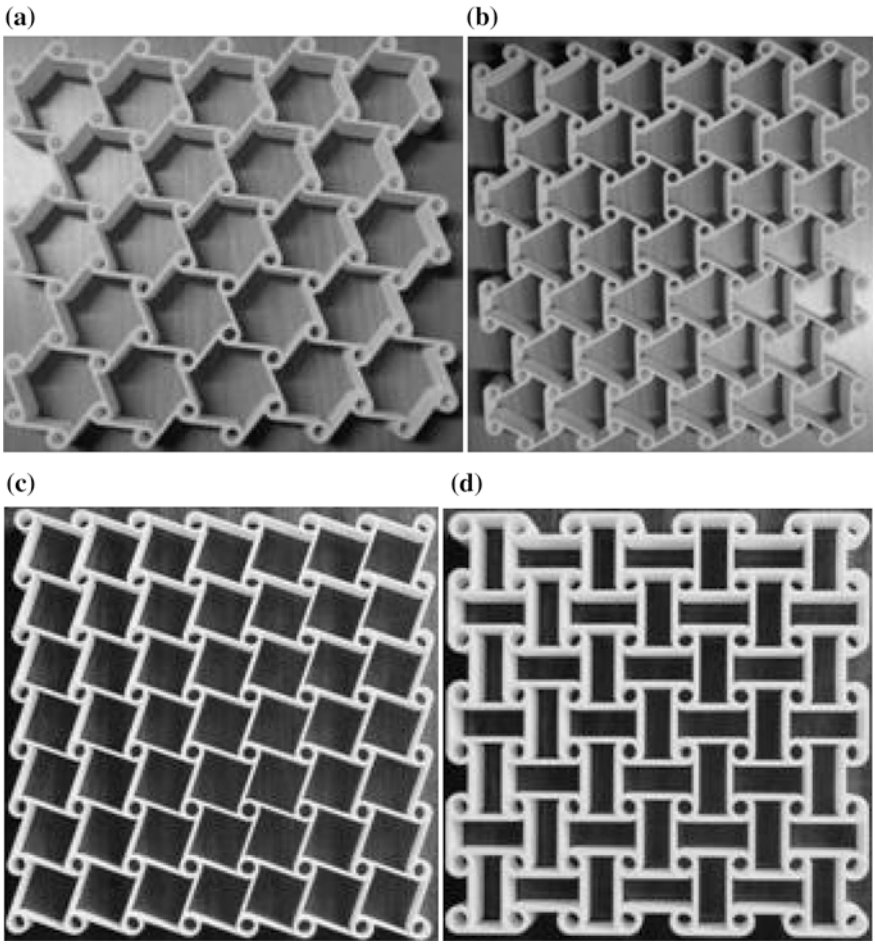

Fig. 2.10.6 Rapid prototype chiral honeycombs investigated: **a** trichiral; **b** anti-trichiral; **c** tetrachiral; and **d** anti-tetrachiral, in the study by Alderson et al. (2010b). With kind permission from Elsevier

where

$$\phi = \cos^{-1}(1 - \beta) \tag{2.10.16}$$

and the dimensionless parameters are defined as

$$\begin{Bmatrix} \alpha_x \\ \alpha_y \\ \beta \\ \gamma \end{Bmatrix} = \frac{1}{r} \begin{Bmatrix} L_x \\ L_y \\ t \\ b \end{Bmatrix} \tag{2.10.17}$$

in which E_c is the Young's modulus of the core material and b is the cell depth.

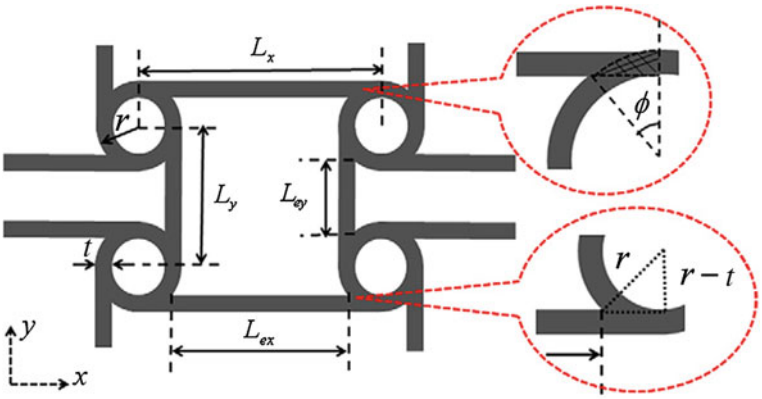

Fig. 2.10.7 Geometry of the anti-tetrachiral anisotropic honeycomb unit cell by Chen et al. (2013). With kind permission from Elsevier

For equal ligament length ($\alpha_x = \alpha_y = \alpha$), Eqs. (2.10.12)–(2.10.15) reduce to $\nu_{xy} = -1$,

$$E_x = E_y = \frac{E_c \beta^3}{6(1-\beta/2)^2}\left(\frac{1}{\alpha - 2\sqrt{2\beta - \beta^2}}\right) \tag{2.10.18}$$

and

$$E_z = \frac{\beta[2\alpha + \pi(2-\beta)] - 2[\phi - (1-\beta)\sin\phi]}{\alpha^2} E_c. \tag{2.10.19}$$

Figure 2.10.8a shows the FE model for comparison with the analytical model, while the experimental procedure is graphically summarized in Fig. 2.10.8b, in which more details are described by Chen et al. (2013). Figure 2.10.9 furnishes the analytical and FE results of the Poisson's ratio by Chen et al. (2013). This, and other results contained therein, presents a parametric analysis showed that one can expect large variations of the in-plane negative Poisson's ratios through changing the length of the ligaments along the x and y directions, and hence provides overall guidelines to develop and manufacture a new type of core for sandwich structures for a variety of engineering applications.

By using finite element simulation, Pozniak and Wojciechowski (2014) determined the Poisson's ratio of anti-chiral structures built on rectangular lattices with disorder introduced by stochastic distributions of circular node sizes. Their investigated models were parameterized by the lattice anisotropy, the rib thickness, and the radii distribution of circular nodes. In this investigation, Pozniak and Wojciechowski (2014) developed three approaches. In the first approach, exact in the limit of infinitely large system and infinitely dense mesh, uses only planar elements (CPS3). Two other approaches are approximate and exploit one-dimensional

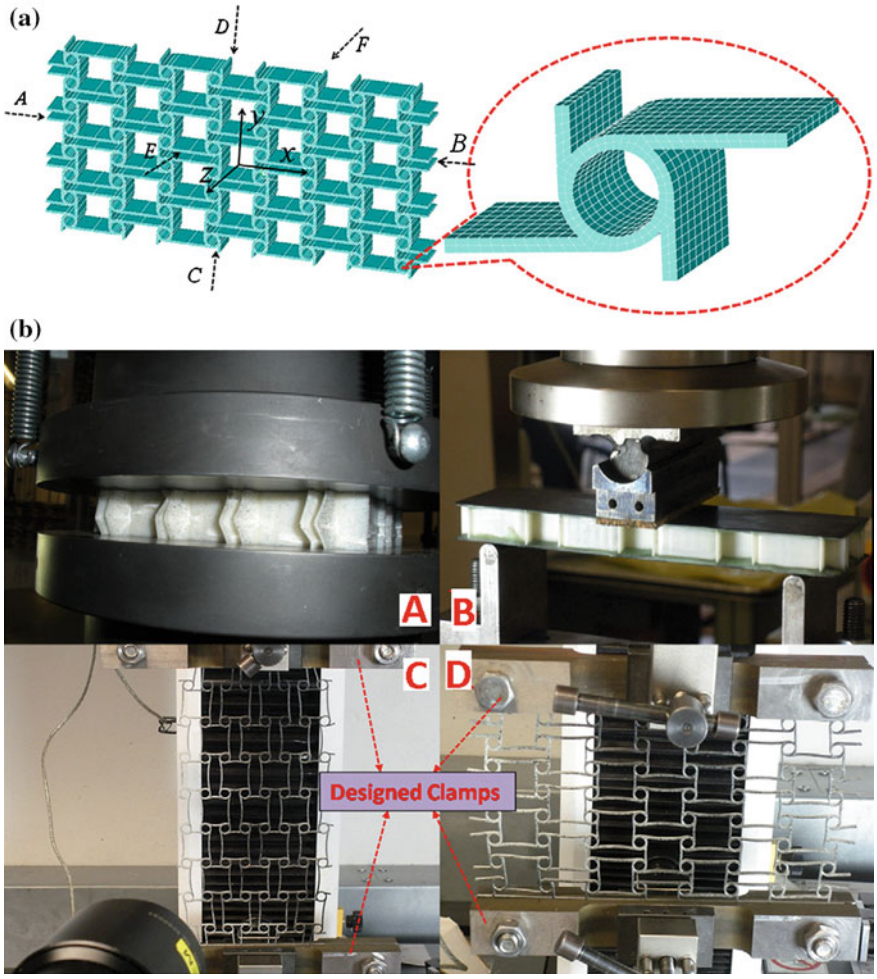

Fig. 2.10.8 **a** Finite element model of repeating unit cell layout, and **b** honeycomb structures experimental setup: (*A*) flatwise compression tests; (*B*) three-point bending tests; (*C*) and (*D*) tensile tests by Chen et al. (2013). With kind permission from Elsevier

elements utilizing the Timoshenko beam theory. Pozniak and Wojciechowski (2014) showed that in the case of sufficiently large anisotropy of the studied structures PR can be highly negative, reaching any negative value, including those lower than −1, and that thin ribs and thin-walled circular nodes favor low values of Poisson's ratio, i.e. in the case of thick ribs and thick-walled circular nodes the Poisson's ratio is higher. In both cases the dispersion of the values of circular nodes radii has a minor effect on the lowest values of PR. A comparison of the results obtained with three different approaches shows that the Timoshenko beam based approximations are valid only in the thin rib limit, i.e. the difference between them grows with increasing thickness (Pozniak and Wojciechowski 2014).

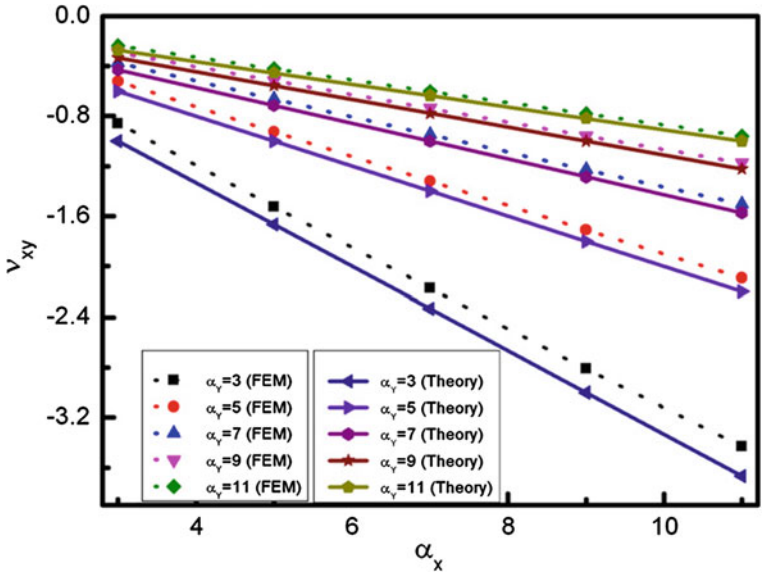

Fig. 2.10.9 FE homogenization and theoretical predictions related to the Poisson's ratio ν_{xy} versus α_x for different α_y by Chen et al. (2013). With kind permission from Elsevier

The effects of hierarchy on the in-plane elastic properties of honey combs have been examined by Taylor et al. (2011), in which the effects of adding hierarchy into a range of honeycombs, with hexagonal, triangular or square geometry super and sub-structure cells, were explored by finite element simulation. It was found that a negative Poisson's ratio sub-structure engenders substantial increases to the density modulus versus conventional honeycombs—partial result of this work is summarized in Fig. 2.10.10.

2.11 Interlocking Hexagons Model

Using the interlocking hexagons model shown in Fig. 2.11.1a, Ravirala et al. (2007) developed a micromechanical model that exhibits auxetic behavior. In addition to the geometries, the adoption of spring constants, as shown in Fig. 2.11.1b, aids the development of the Young's moduli expressions. While a hexagonal array of honeycomb with hexagonal and re-entrant structures give conventional and auxetic behavior respectively, a hexagonal array of interlocking hexagonal and re-entrant structures give auxetic and conventional behavior, respectively. See Fig. 2.11.1c for the interlocking re-entrant structure.

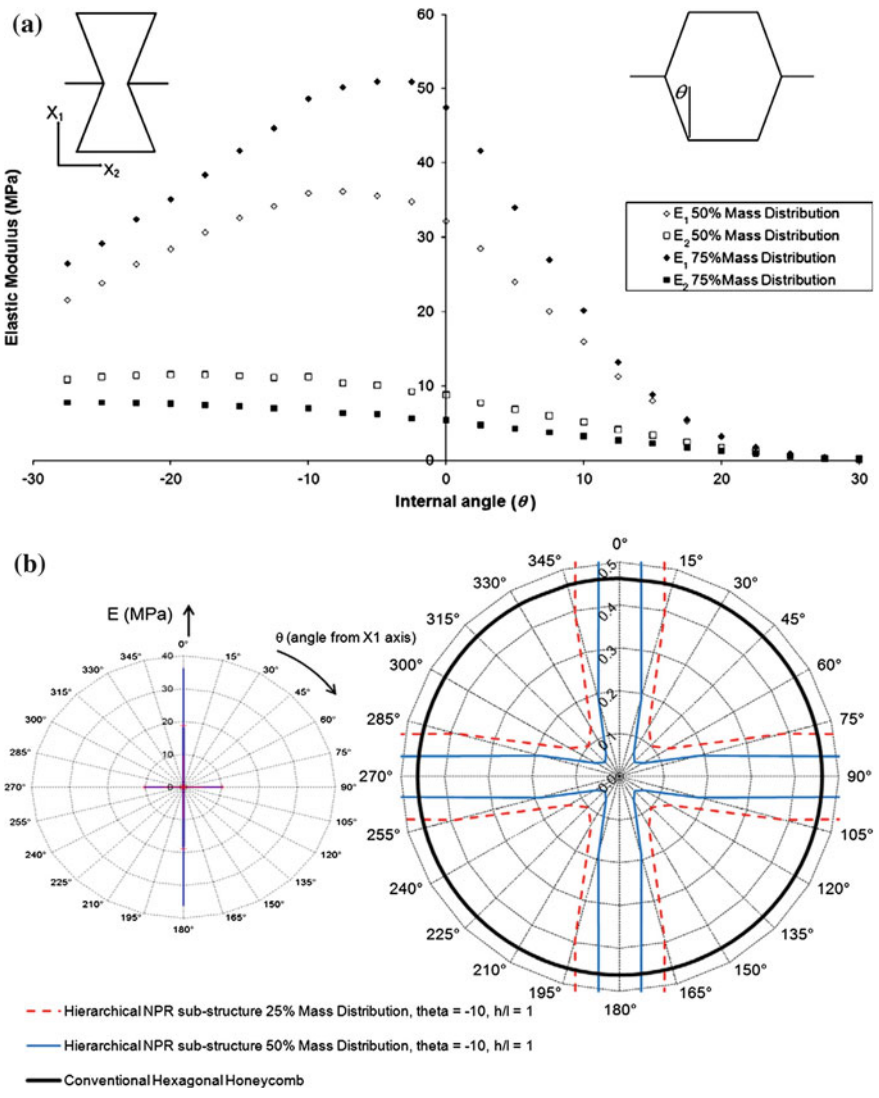

Fig. 2.10.10 **a** The internal angle of the substructure versus the elastic moduli E_1 and E_2 (referring to the X_1 and X_2 axes) for 50 % mass distribution (*open symbols*) and 75 % mass distribution within the sub-structure (*closed symbols*). For all cases θ in the super-structure was 30°. **b** The anisotropy present in re-entrant hierarchical structures shown by a polar plot of the Young's modulus versus loading angle for two hierarchical honeycombs with a NPR sub-structures (θ = −10°), with mass distributions of 50 and 25 % respectively. A conventional hexagonal honeycomb is shown for comparison (Taylor et al. 2011). With kind permission from Elsevier

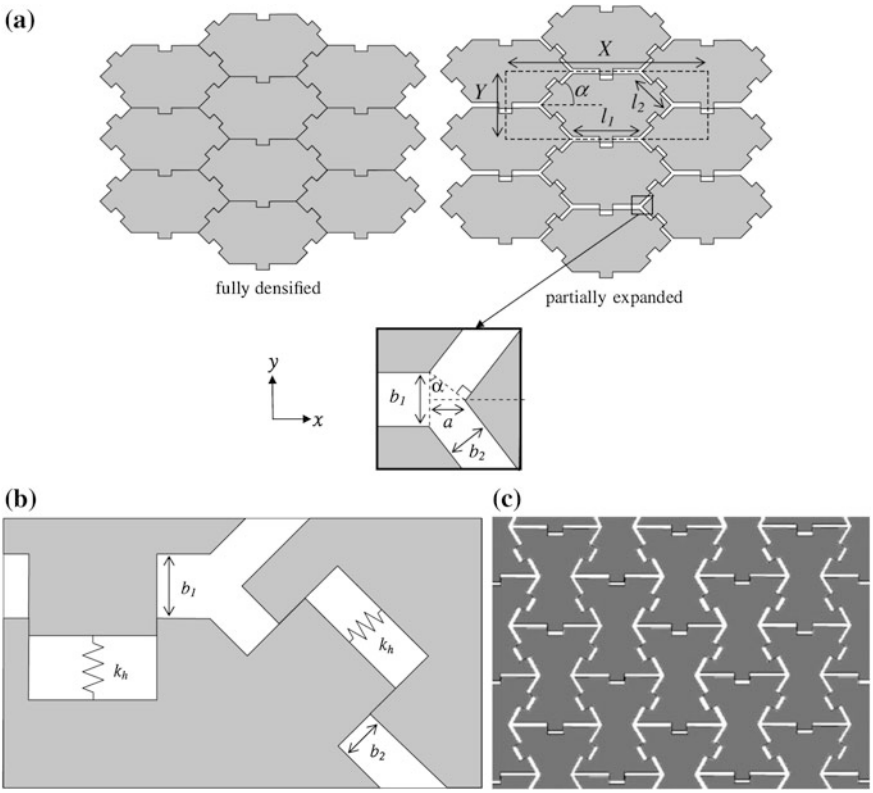

Fig. 2.11.1 **a** Auxetic behavior from interlocking hexagon structure, **b** spring connections, and **c** conventional behavior from interlocking re-entrant structure (Ravirala et al. 2007). With kind permission from Springer Science+Business Media

Based on the geometrical parameters given in Fig. 2.11.1a, the elastic moduli established by Ravirala et al. (2007) are

$$v_{xy} = \frac{1}{v_{yx}} = -\frac{(l_1 + l_2\cos\alpha + a)\cos\alpha}{l_2\sin^2\alpha + a\cos\alpha} \tag{2.11.1}$$

$$E_x = k_h\left(\frac{2\cos^2\alpha + 1}{\sin\alpha}\right)\left(\frac{l_1 + l_2\cos\alpha + a}{l_2\sin^2\alpha + a\cos\alpha}\right) \tag{2.11.2}$$

$$E_y = k_h\left(\frac{2\cos^2\alpha + 1}{\sin\alpha\cos^2\alpha}\right)\left(\frac{l_2\sin^2\alpha + a\cos\alpha}{l_1 + l_2\cos\alpha + a}\right) \tag{2.11.3}$$

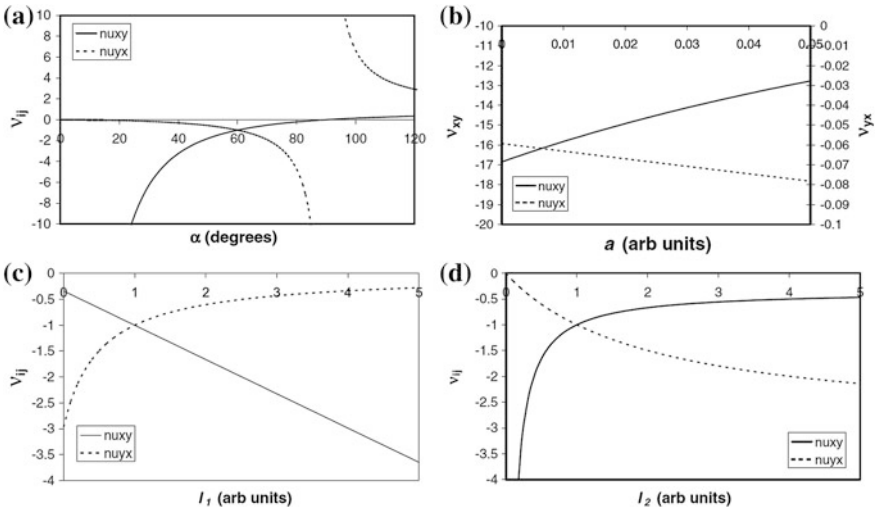

Fig. 2.11.2 Poisson's ratio as functions of: **a** angle α ($l_1 = l_2 = 1$; $a = 0.01$), **b** gap parameter a ($\alpha = 30°$; $l_1 = 2$; $l_2 = 0.5$), **c** edge length l_1 ($\alpha = 60°$; $l_2 = 1$; $a = 0.01$), and **d** edge length l_2 ($\alpha = 60°$; $l_1 = 1$; $a = 0.01$) plotted by Ravirala et al. (2007). With kind permission from Springer Science+Business Media

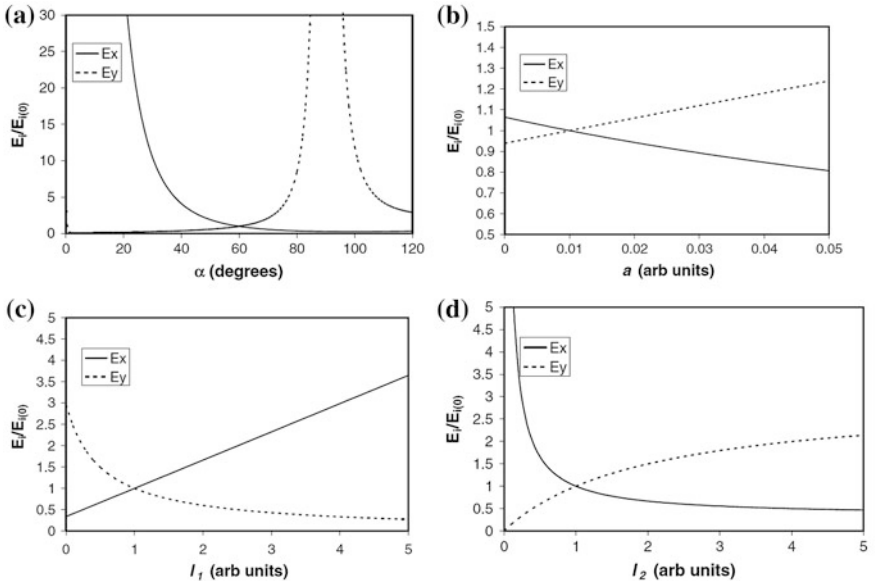

Fig. 2.11.3 Young's moduli as functions of: **a** angle α ($l_1 = l_2 = 1$; $a = 0.01$), **b** gap parameter a ($\alpha = 30°$; $l_1 = 2$; $l_2 = 0.5$), **c** edge length l_1 ($\alpha = 60°$; $l_2 = 1$; $a = 0.01$), and **d** edge length l_2 ($\alpha = 60°$; $l_1 = 1$; $a = 0.01$) plotted by Ravirala et al. (2007). With kind permission from Springer Science+Business Media

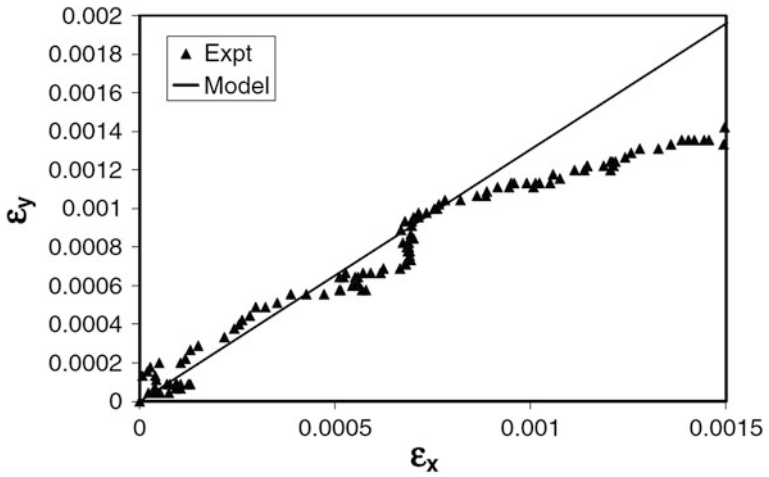

Fig. 2.11.4 Comparison between experimental results by Ravirala et al. (2005) and the interlocking hexagons model with $l_1/l_2 = 2.86$ and $\alpha = 69.2°$ (Ravirala et al. 2007). With kind permission from Springer Science+Business Media

where the spring stiffness constant, k_h, is shown in Fig. 2.11.1b. It can be easily seen that

$$v_{xy}E_y = v_{yx}E_x = -k_h\left(\frac{2\cos^2\alpha + 1}{\sin\alpha\cos\alpha}\right) \tag{2.11.4}$$

and that substitution of $l_1 = l_2$ and $\alpha = 60°$ into Eq. (2.11.1) and (2.11.4) reduces them to $v_{xy} = v_{yx} = -1$ and $v_{xy}E_y = v_{yx}E_x = -2k_h\sqrt{3}$.

Figures 2.11.2 and 2.11.3 show the plots of Poisson's ratio and Young's moduli, respectively, for various combinations of edge lengths l_1, l_2, gap parameter a, and the angle α, using Eqs. (2.11.1)–(2.11.3). Comparison with

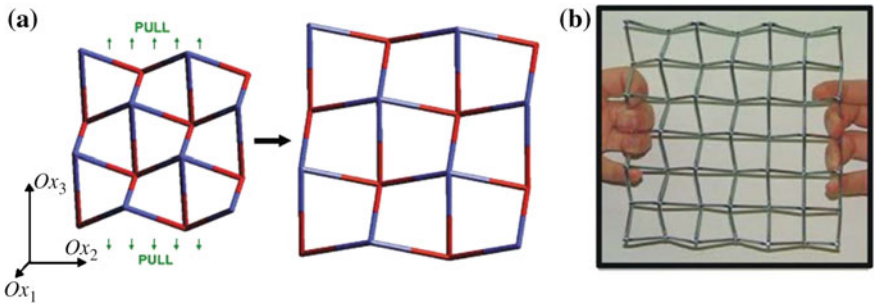

Fig. 2.12.1 **a** Schematic diagram of the model macrostructure, and **b** a photograph of the commercially manufactured 'egg rack' structure with the same geometry by Grima et al. (2005). With kind permission from The Royal Society of Chemistry

(a)

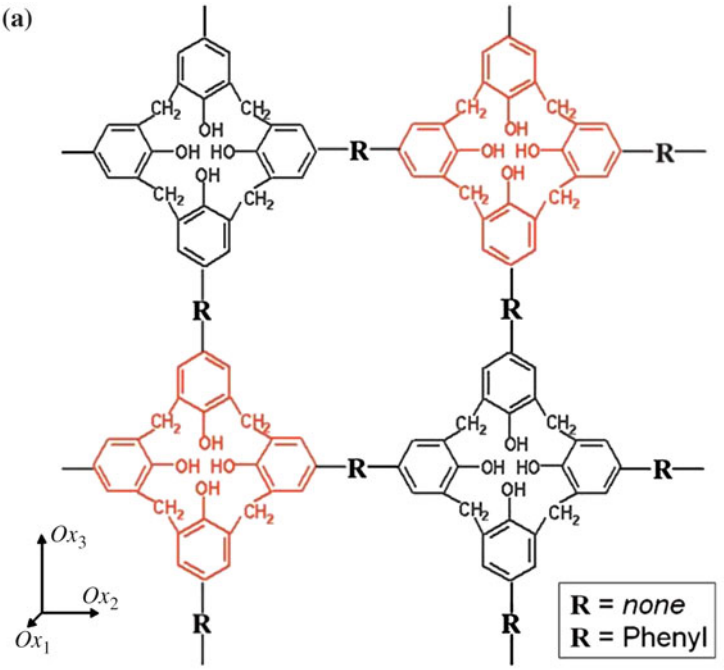

(b)

Structure	Mathematical model for macrostructure	R = none	R = phenyl
v_{12}	+1	0.36	0.52
v_{21}	+1	1.42	1.18
v_{13}	+1	0.36	0.52
v_{31}	+1	1.42	1.18
v_{23}	−1	−0.51	−0.87
v_{32}	−1	−0.51	−0.85
E_1	*n/a*	4.63	1.66
E_2	*n/a*	18.10	3.78
E_3	*n/a*	18.10	3.78

Fig. 2.12.2 **a** The structural formulae of the repeat units for the molecular 'double calix' structures, and **b** the simulated single crystalline Poisson's ratios (v_{ij}) and Young's moduli (E_i) of the two molecular systems (**a**) and those predicted for the idealized folded macrostructure shown in Fig. 2.12.1 (Grima et al. 2005). With kind permission from The Royal Society of Chemistry

experimental results by Ravirala et al. (2005) gives the fitted results $l_1/l_2 = 2.86$ and $\alpha = 69.2°$. The predicted transverse total true strain (ε_y) versus axial total true strain (ε_x) for $l_1/l_2 = 2.86$ and $\alpha = 69.2°$ assuming an initially fully dense structure (i.e. $a = 0$ for the undeformed structure) is shown in Fig. 2.11.4. Also shown, for comparison, is the experimental transverse versus axial (extrusion) total true strain

data by Ravirala et al. (2005) assuming the extrusion direction corresponds to the model *x*-direction. Combining the hexagonal shape of nodules in this section with the re-entrant fibrils discussed in Sects. 2.3 and 2.4, Lim and Acharya U (2009) proposed a hexagonal array of fourfold interconnected hexagonal nodules for modeling auxetic microporous polymers in 2D and 3D.

2.12 Egg Rack Structure

Based on an "egg rack" structure, shown in Fig. 2.12.1, Grima et al. (2005) proved the auxeticity of networked calix[4]arene polymers using molecular simulation (Fig. 2.12.2).

References

Abramovitch H, Burgard M, Edery-Azulay L, Evans KE, Hoffmeister M, Miller W, Scarpa F, Smith CW, Tee KF (2010) Smart tetrachiral and hexachiral honeycomb: sensing and impact detection. Compos Sci Technol 70(7):1072–1079

Alderson KL, Neale PJ (1994) Private communication

Alderson A, Evans KE (1995) Microstructural modelling of auxetic microporous polymers. J Mater Sci 30(13):3319–3332

Alderson A, Evans KE (1997) Modelling concurrent deformation mechanisms in auxetic microporous polymers. J Mater Sci 32(11):2797–2809

Alderson KL, Alderson A, Evans KE (1997) The interpretation of the strain-dependent Poisson's ratio in auxetic polyethylene. J Strain Anal Eng Des 32(3):201–212

Alderson A, Evans KE (2001) Rotation and dilation deformation mechanisms for auxetic behavior in the α-cristobalite tetrahedral framework structure. Phys Chem Miner 28(10):711–718

Alderson A, Alderson KL, Chirima G, Ravirala N, Zied KM (2010a) The in-plane linear elastic constants and out-of-plane bending of 3-coordinated ligament and cylinder-ligament honeycombs. Compos Sci Technol 70(7):1034–1041

Alderson A, Alderson KL, Attard D, Evans KE, Gatt R, Grima JN, Miller W, Ravirala N, Smith CW, Zied K (2010b) Elastic constants of 3-, 4- and 6-connected chiral and anti-chiral honeycombs subject to uniaxial in-plane loading. Compos Sci Technol 70(7):1042–1048

Branka AC, Pieranski P, Wojciechowski KW (1982) Rotatory phase in a system of hard cyclic hexamers; an experimental modelling study. J Phys Chem Solids 43(9):817–818

Caddock BD, Evans KE (1989) Microporous materials with negative Poisson's ratios I: microstructure and mechanical properties. J Phys D Appl Phys 22(12):1877–1882

Chen YJ, Scarpa F, Liu YJ, Leng JS (2013) Elasticity of anti-tetrachiral anisotropic lattices. Int J Solids Struct 50(6):996–1004

Chetcuti E, Ellul B, Manicaro E, Brincat JP, Attard D, Gatt R, Grima JN (2014) Modeling auxetic foams through semi-rigid rotating triangles. Phys Status Solidi B 251(2):297–306

Choi JB, Lakes RS (1992) Non-linear properties of polymer cellular materials with a negative Poisson's ratio. J Mater Sci 27(19):5375–5381

Choi JB, Lakes RS (1995) Nonlinear analysis of the Poisson's ratio of negative Poisson's ratio foams. J Compos Mater 29(1):113–128

Evans KE, Nkansah MA, Hutchinson IJ, Rogers SC (1991) Molecular network design. Nature 353 (6340):124

Gaspar N, Ren XJ, Smith CW, Grima JN, Evans KE (2005) Novel honeycombs with auxetic behavior. Acta Mater 53(8):2439–2445
Gaspar N, Smith CW, Alderson A, Grima JN, Evans KE (2011) A generalised three-dimensional tethered-nodule model for auxetic materials. J Mater Sci 46(2):372–384
Gibson LJ, Ashby MF (1988) Cellular solids: structure and properties. Pergamon Press, Oxford
Grima JN, Evans KE (2000) Auxetic behavior from rotating squares. J Mater Sci Lett 19 (17):1563–1565
Grima JN, Alderson A, Evans KE (2004) Negative Poisson's ratios from rotating rectangles. Comput Methods Sci Technol 10(2):137–145
Grima JN, Williams JJ, Evans KE (2005) Networked calix[4]arene polymers with unusual mechanical properties. Chem Commun 32:4065–4067
Grima JN, Evans KE (2006) Auxetic behavior from rotating triangles. J Mater Sci 41(10):3193–3196
Grima JN, Zammit V, Gatt R, Alderson A, Evans KE (2007) Auxetic behavior from rotating semi-rigid units. Phys Status Solidi B 244(3):866–882
Grima JN, Farrugia PS, Caruana C, Gatt R, Attard D (2008) Auxetic behavior from stretching connected squares. J Mater Sci 43(17):5962–5971
Grima JN, Gatt R, Ellul B, Chetcuti E (2010) Auxetic behavior in non-crystalline materials having star or triangular shaped perforations. J Non-Cryst Solids 356(37–40):1980–1987
Grima JN, Manicaro E, Attard D (2011) Auxetic behavior from connected different-sized squares and rectangles. Proc R Soc A 467(2126):439–458
Grima JN, Chetcuti E, Manicaro E, Attard D, Camilleri M, Gatt R, Evans KE (2012) On the auxetic properties of generic rotating rigid triangles. Proc R Soc A 468(2139):810–830
Kopyt P, Damian R, Celuch M, Ciobanu R (2010) Dielectric properties of chiral honeycombs—modelling and experiment. Compos Sci Technol 70(7):1080–1088
Lim TC, Acharya UR (2009) An hexagonal array of fourfold interconnected hexagonal nodules for modeling auxetic microporous polymers: a comparison of 2D and 3D. J Mater Sci 44:4491-4494
Lim TC, Alderson A, Alderson KL (2014) Experimental studies on the impact properties of auxetic materials. Phys Status Solidi B 251(2):307–313
Lorato A, Innocenti P, Scarpa F, Alderson A, Alderson KL, Zied KM, Ravirala N, Miller W, Smith CW, Evans KE (2010) The transverse elastic properties of chiral honeycombs. Compos Sci Technol 70(7):1057–1063
Michelis P, Spitas V (2010) Numerical and experimental analysis of a triangular auxetic core made of CFR-PEEK using the directionally reinforced integrated single-yarn (DIRIS) architecture. Compos Sci Technol 70(7):1064–1071
Masters IG, Evans KE (1996) Models for the elastic deformation of honeycombs. Compos Struct 35(4):403–422
Miller W, Smith CW, Scarpa F, Evans KE (2010) Flatwise buckling optimization of hexachiral and tetrachiral honeycombs. Compos Science Technol 70(7):1049–1056
Milton GW (1992) Composite materials with Poisson's ratio close to -1. J Mech Phys Solids 40 (5):1105–1137
Nakamura S, Lakes RS (1995) Finite element analysis of Saint-Venant end effects in micropolar elastic solids. Eng Comput 12(6):571–587
Neale PJ, Alderson KL, Pickles AP, Evans KE (1993) Negative Poisson's ratio of microporous polyethylene in compression. J Mater Sci Lett 12(19):1529–1532
Pozniak AA, Smardzewski J, Wojciechowski KW (2013) Computer simulations of auxetic foams in two dimensions. Smart Mater Struct 22(8):084009
Pozniak AA, Wojciechowski KW (2014) Poisson's ratio of rectangular anti 0-chiral structures with size dispersion of circular nodes. Phys Status Solidi B 251(2):367–374
Prall D, Lakes RS (1997) Properties of a chiral honeycomb with a Poisson's ratio of -1. Int J Mech Sci 39(3):305–314
Ravirala N, Alderson A, Alderson KL, Davies PJ (2005) Auxetic polypropylene films. Polym Eng Sci 45(4):517–528

Ravirala N, Alderson A, Alderson KL (2007) Interlocking hexagon model for auxetic behavior. J Mater Sci 42(17):7433–7445

Rothenburg L, Berlin AA, Bathurst RJ (1991) Microstructure of isotropic materials with negative Poisson's ratio. Nature 354(6353):470–472

Smith CW, Grima JN, Evans KE (2000) A novel mechanism for generating auxetic behavior in reticulated foams: missing rib foam model. Acta Mater 48(17):4349–4356

Spadoni A, Ruzzene M, Gonella S, Scarpa F (2009) Phononic properties of hexagonal chiral lattices. Wave Motion 46(7):435–450

Spadoni A, Ruzzene M (2012) Elasto-static micro polar behavior of a chiral auxetic lattice. J Mech Phys Solids 60(1):156–171

Taylor CM, Smith CW, Miller W, Evans KE (2011) The effects of hierarchy on the in-plane elastic properties of honeycombs. Int J Solids Struct 48(9):1330–1339

Taylor M, Francesconi L, Gerendas M, Shanian A, Carson C, Bertoldi K (2013) Low porosity metallic periodic structures with negative Poisson's ratio. Adv Mater 26(15):2365–2370

Wojciechowski KW (1987) Constant thermodynamic tension Monte-Carlo studies of elastic properties of a two-dimensional system of hard cyclic hexamers. Mol Phys 61(5):1247–1258

Wojciechowski KW (1989) Two-dimensional isotropic system with a negative Poisson ratio. Phys Lett A 137(1,2):60–64

Wojciechowski KW, Branka AC (1989) Negative Poisson ratio in a two-dimensional ''isotropic'' solid. Phys Rev A 40(12):7222–7225

Wojciechowski KW (2003) Remarks on "Poisson ratio beyond the Limits of the elasticity theory". J Phys Soc Jpn 72(7):1819–1820

Yang DU, Huang FY (2001) Analysis of Poisson's ratio for a micropolar elastic rectangular plate using finite element method. Eng Comput 18(7):1012–1030

http://www.springer.com/978-981-287-274-6

Auxetic Materials and Structures
Lim, T.-C.
2015, XV, 587 p. 375 illus., 60 illus. in color., Hardcover
ISBN: 978-981-287-274-6